SYNTHESIS AND INVESTIGATION OF QUINONE-PYRROLE POLYMERIC MATERIALS FOR ZINC-ION BATTERIES

A Thesis Submitted to the
Graduate School of
İzmir Institute of Technology
in Partial Fulfillment of the Requirements for the Degree of

MASTER OF SCIENCE

in Chemistry

by
Utku Cem ÇANAKÇI

July 2024
İZMİR

We approve the thesis of **Utku Cem ÇANAKÇI**

Examining Committee Members:

Prof. Dr. Armağan Kinal
Department of Chemistry, Ege University

Assoc. Prof. Dr. Ümit Hakan Yıldız
Department of Chemistry, İzmir Institute of Technology

Assist. Prof. Dr. Onur Büyükçakır
Department of Chemistry, İzmir Institute of Technology

5 July 2024

Assist. Prof. Dr. Onur Büyükçakır
Supervisor, Department of Chemistry
İzmir Institute of Technology

Prof. Dr. Gülşah Şanlı Mohamed
Head of the Department of Chemistry

Prof. Dr. Mehtap EANES
Dean of the Graduate School

ACKNOWLEDGMENTS

As I begin this section, I would like to thank Dr. Onur Büyükçakır, who I believe has positively impacted many aspects of my life. It was a great privilege and honor for me to work with a scientist like him.

I would like to thank every member of the Büyükçakır Research Group, with whom I had the honor of working and being a part of. I am deeply grateful to Yasmin Geçalp, Yaren Naz Erözen, Gizem Şimşek, Mustafa Erdoğmuş, Ferit Begar, Batu Sercan Cantürk, Betül Akkuş, and Hüseyin Zeybek for their endless friendship and beautiful hearts.

I want to thank my friends, Süleyman Pişken and Nisa Yıldırım, for their wonderful friendship and the countless memories we've shared.

I am grateful to the committee members, Assoc. Prof. Ümit Hakan Yıldız and Prof. Dr. Armağan Kinal, for their time and support.

Even though I know my thanks will never be enough, I want to express my deepest gratitude to my father, Mustafa Çanakçı, and my mother, Rabia Çanakçı. With all the love and affection in my heart, I thank them for believing in me and always standing behind me. Additionally, I am deeply thankful to my sister Mine Özden Çanakçı, for all the support she has given me and continues to provide every day. She is the greatest blessing of my life and will forever remain so. Living as an individual raised by them will always bring me infinite honor.

The study is funded by the Scientific and Technical Research Council of Turkey, TÜBİTAK Project No: 220Z024.

ABSTRACT

SYNTHESIS AND INVESTIGATION OF QUINONE-PYRROLE POLYMERIC MATERIALS FOR ZINC-ION BATTERIES

The widespread use of fossil fuels today has a devastating effect on the environment. This situation necessitates the adoption of environmentally friendly alternative energy sources. Zinc-ion batteries represent a new, developing class of energy storage systems with significant potential in this regard. However, a major challenge in advancing this technology is developing efficient and reversible cathode materials that can accommodate Zn^{2+} ions. Quinone-based conjugated polymeric materials are excellent cathode choices for zinc-ion batteries due to their redox-active structures, easily modifiable structures, and strong chemical and thermal stability.

This study synthesized two quinone-based redox-active polymers (QRPs) as cathode materials for zinc-ion batteries (ZIBs). The inherent properties of QRPs ensure effective Zn^{2+} diffusion into their redox centers, guaranteeing long-term cycling stability. QRP-1 and QRP-2 cathodes delivered discharge capacities of 180 mA h g^{-1} and 134 mA h g^{-1}, respectively, at 0.1 mA g^{-1}. Remarkably, QRPs maintained long-term cycling stability at 2.0 A g^{-1} over 10000 cycles, with final specific capacities of 42 mA h g^{-1} for QRP-1 and 104 mA h g^{-1} for QRP-2. We believe that this work demonstrates the potential of quinone-based conjugated polymeric materials as effective cathode materials for zinc-ion batteries and will attract the attention of energy storage researchers.

ÖZET

ÇİNKO-İYON PİLLER İÇİN KİNON-PİROL POLİMERİK MALZEMELERİN SENTEZİ VE İNCELENMESİ

Fosil yakıtların günümüzde yaygın kullanımı çevre üzerinde yıkıcı bir etkiye sahiptir. Bu durum, çevre dostu alternatif enerji kaynaklarının benimsenmesini zorunlu kılmıştır. Çinko-iyon piller, bu bağlamda önemli potansiyele sahip, gelişmekte olan yeni bir enerji depolama sistemi sınıfını temsil etmektedir. Bununla birlikte, bu teknolojiyi ilerletmekteki büyük zorluk, Zn^{2+} iyonlarını verimli ve geri dönüşümlü olarak barındırabilen katot malzemeleri geliştirmektir. Kinon bazlı konjuge polimerik malzemeler, redoks aktif yapıları, kolayca değiştirilebilen yapıları ve güçlü kimyasal ve termal kararlılıkları nedeniyle çinko-iyon pilleri için mükemmel katot seçenekleridir.

Bu çalışmada, çinko-iyon pilleri (ÇİP'ler) için katot malzemeleri olarak kinon-pirol konjuge polimerik malzemeler (QRP'ler) sentezlendi. QRP'lerin içsel özellikleri, redoks merkezlerine etkili Zn^{2+} difüzyonunu kolaylaştırarak uzun vadeli döngü kararlılığını sağlar. QRP-1 ve QRP-2 sırasıyla 0.1 mA g^{-1} akım yoğunluğunda 180 mA h g^{-1} ve 134 mA h g^{-1} deşarj kapasitesi gösterdi. QRP'ler, 2.0 A g^{-1} akım yoğunluğunda 10000 döngü boyunca olağanüstü döngü kararlılığı göstererek, QRP-1 ve QRP-2 için sırasıyla 42 mA h g^{-1} ve 104 mA h g^{-1} olmak üzere oldukça yüksek final kapasiteleri elde edildi. Bu çalışmanın, kinon bazlı konjuge polimerik malzemelerin çinko-iyon piller için etkili katot malzemeleri olarak potansiyelini gösterdiğine ve enerji depolama alanında çalışan araştırmacılarının dikkatini çekeceğine inanıyoruz.

TABLE OF CONTENTS

LIST OF FIGURES

Figure **Page**

LIST OF ABBREVIATIONS

ZIBs	Zinc-ion Batteries
LIBs	Lithium-ion Batteries
^1H	Proton Nuclear Magnetic Resonance Spectroscopy
CV	Cyclic Voltammetry
GCD	Galvanostatic Charge and Discharge Measurements
^{13}C	Carbon Nuclear Magnetic Resonance Spectroscopy
FTIR	Fourier- Transform Infrared Spectroscopy
CAN	Cerium Ammonium Nitrate
DMF	N,N'-Dimethylformamide
NMR	Nuclear Magnetic Resonance
SEM	Scanning Electron Microscopy
TGA	Thermogravimetric Analysis
PXRD	Powder X-ray Diffraction Analysis
XPS	X-ray Photoelectron Spectroscopy
EtOH	Ethanol
CH_3CN	Acetonitrile
BET	Brunauer-Emmett-Teller
MeOH	Methanol
CDCl3	Deuterated chloroform
IUPAC	International Union of Pure and Applied Chemistry
DCM	Dichloromethane
DMSO-d_6	Deuterated dimethyl sulfoxide
THF	Tetrahydrofuran
s	Singlet
d	Doublet
t	Triplet
m	Multiplet
dd	Doublet of Doublet

CHAPTER 1

INTRODUCTION

1.1. Energy Storage

The most significant question mark of the 21st century is the problems in energy storage. The rapid depletion of fossil fuels and the disastrous effects of their widespread usage on the environment necessitate their replacement with alternative energy sources.[1] This trend promotes the innovative use of energy. Considering all these, finding new ways for clean and efficient energy use has become necessary. Currently, academic studies on this issue are having a significant influence.

The history of energy storage dates back to the early periods of humanity and has shown significant developments. In early times, humans stored energy in natural forms; For example, they lit a fire using biomass carriers such as wood and coal. Using these techniques, humans utilize energy to heat, cook food, and provide light to the environment. During the Industrial Revolution, humans used coal to power steam engines, which enabled electricity production. Over the past few decades, the utilization of alternate energy sources such as hydroelectricity, nuclear power, and fossil fuels for electricity generation has become prevalent.[2]

The increasing availability of renewable energy has increased the significance of electrical energy storage. Batteries are the most crucial energy storage devices in use today. Lithium-ion batteries possess the most elevated energy density available in the industry. Due to their extended lifespan, they are used in various items, ranging from mobile phones to electric cars.[3] Creating new energy storage methods is essential to develop more productive and sustainable energy. These methods are gradually created by combining different factors or energy usage patterns, which require solutions to countries' environmental challenges.[4]

1.2. Batteries

Voltaic batteries, invented by Alessandro Volta, became the first batteries in 1800 to be used practically.[5] They store electric energy produced by various chemical reactions and allow the utilization of electric devices not connected to a permanent electricity source. Nowadays, batteries are one of the most common sources of electricity in many spheres of the modern world. The most used examples include devices such as cell phones and tablets, and energy consumption commodities are electric cars and special-purpose gadgets like patient monitoring systems.

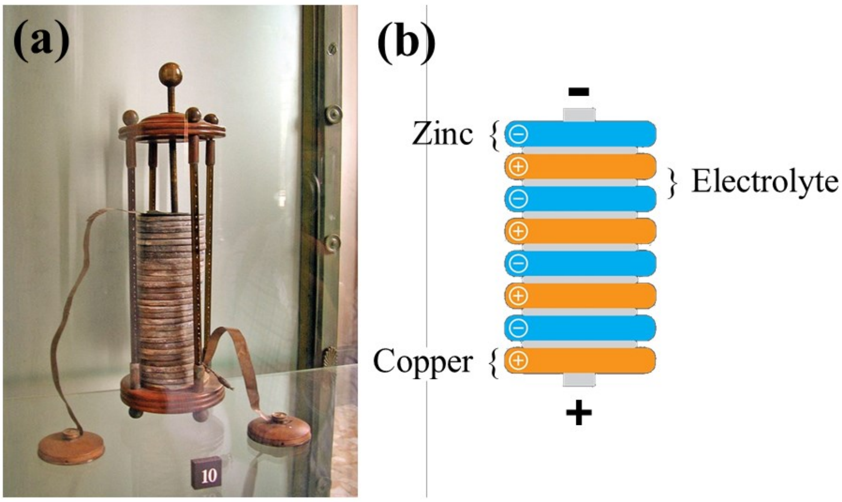

Figure 1.1. (a) A voltaic pile, (b) Schematic diagram of a copper-zinc voltaic pile.

The demand for high-performance rechargeable batteries has become quite visible in recent years. The functions and requirements of batteries are understood in general. Figure 1.2. illustrates that research on batteries has increased significantly in the past 15 years. Articles published on batteries from 2010 to 2017 show a 260% growth in the total volume of battery literature.[6] This number is approximately 4.5 times the general literature increase rate. Although tremendous progress has been made in battery research, the goals of this research have not changed over the years. The main goals are reducing dimensions and weight, lowering costs, and safe use.

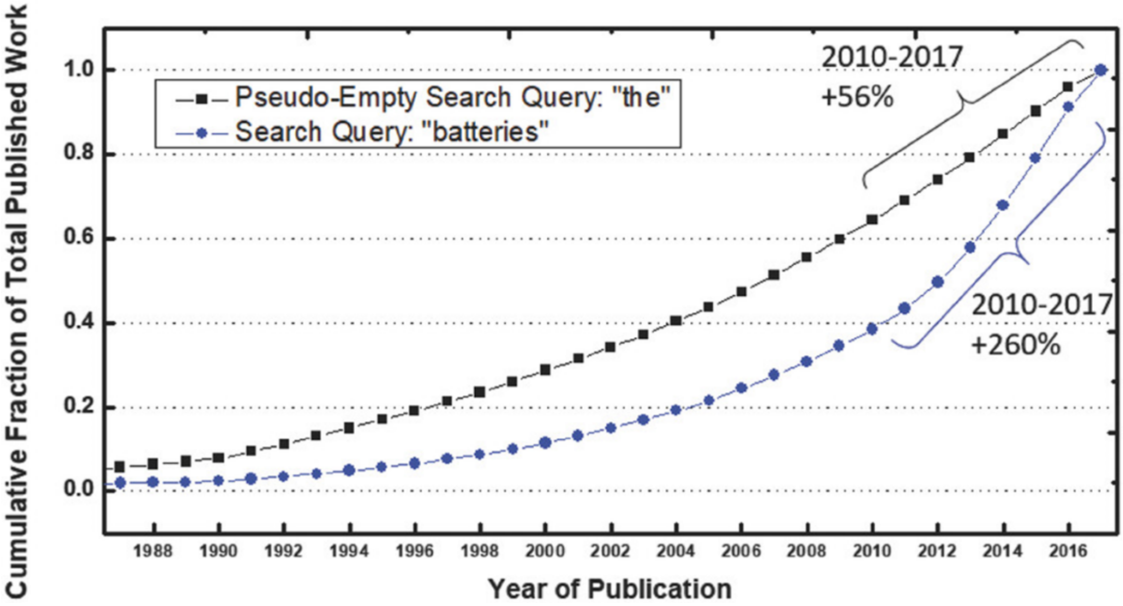

Figure 1.2. Comparison of literature growth from 1987 to 2017.[7]

1.2.1. Lithium-Ion Batteries

Lithium-ion batteries (Li-ion) are the most popular type of rechargeable battery today. These batteries are widely used to power mobile phones, tablets, and electric vehicles. Li-ion batteries are based on a system in which lithium ions move between positive and negative electrodes.[7] Li-ion batteries are well-known for their exceptional energy density.[8] This feature enables them to store significant energy in a small, portable package. Another advantage of these batteries is that they have a better cycle life and are fast charging, in contrast to many other battery types. Also, Li-ion batteries exhibit a low self-discharge rate, indicating their ability to keep their charge for a significant duration of time when not in use. Notably, the fact that Li-ion batteries can be produced in various sizes and shapes gives them versatility for various uses.[9]

Nevertheless, multiple problems might occur with Li-ion batteries. The expense of Li-ion batteries is a major issue. They have a greater beginning expense than other battery varieties. Although Li-ion batteries have a long cycle life, their overall lifespan is relatively limited.[10] Over time, their capacity decreases, which means they may need replacement, adding to the long-term cost. It is important to note that these batteries have the potential to experience thermal runaway, resulting in fires or explosions in severe situations.[11] Also, the extraction of lithium and other rare materials during the production and disposal of Li-ion batteries can result in a substantial environmental effect.[12]

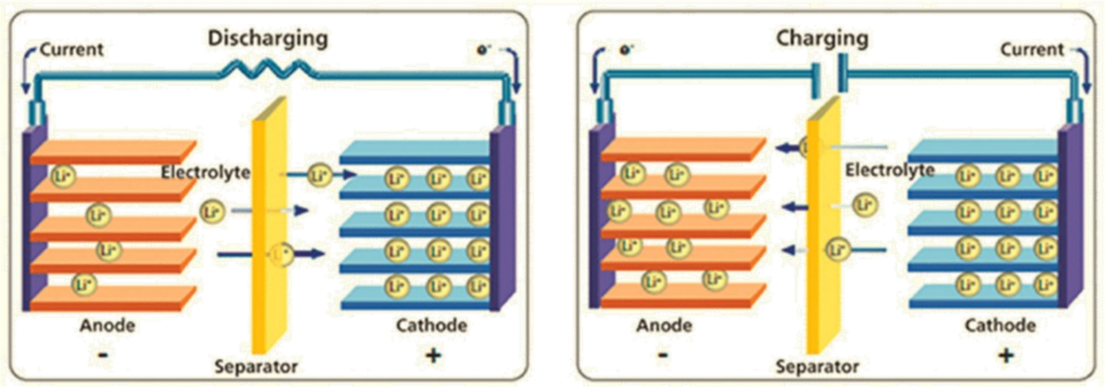

Figure 1.3. Basic working principle of lithium-ion batteries.[13]

Figure 1.3 shows the working mechanism of Li-ion batteries. These batteries' charging and discharging processes are based on the movement of lithium ions between the chemical components of the battery. Lithium ions move from the cathode to the anode during the charging process. This movement allows the battery to store electrical energy as chemical energy. The discharge process takes place exactly the opposite of the charging process. During battery usage, lithium ions shift from the anode to the cathode. Throughout this procedure, the battery converts its accumulated chemical energy into electrical energy, which it then supplies to the connected device.[13]

1.2.2. Zinc-Ion Batteries

The drawbacks of Li-ion batteries led to the development of other metal-ion batteries to be complementary for Li-ion batteries. Considering this situation, Zinc ion batteries (ZIBs) are one of the most promising systems in the search for sustainable and environmentally friendly energy storage systems.[14]

Zinc is a non-toxic and recyclable element, which makes ZIBs environmentally friendly. Furthermore, ZIBs are a significantly safer option than Li-ion battery systems because they can be operated in aqueous electrolytes, even under elevated temperatures, eliminating the potential hazards of explosion or combustion.[15] In addition, the abundant availability of zinc metal contributes to cost reduction. The estimated cost for ZIBs using a zinc anode, a vanadium oxide cathode, and an aqueous $ZnSO_4$ electrolyte is less than \$65 per kilowatt-hour, far more affordable than today's Li-ion batteries costing \$300 per kilowatt-hour (Figure 1.4).[16] Also, ZIBs have garnered significant interest due to metallic zinc's numerous advantages. These include a high theoretical capacity of 820 $mA\ h\ g^{-1}$ or

5851 mA h cm^{-3} and well-balanced kinetics, stability, and reversibility in aqueous solutions.[17] Additionally, ZIBs exhibit a low electrochemical potential of -0.763 V compared to the standard hydrogen electrode (SHE) and a two-electron transfer during the redox reaction, resulting in a high energy density.[17] These advantages demonstrated by ZIBs make them an attractive option for renewable energy systems.

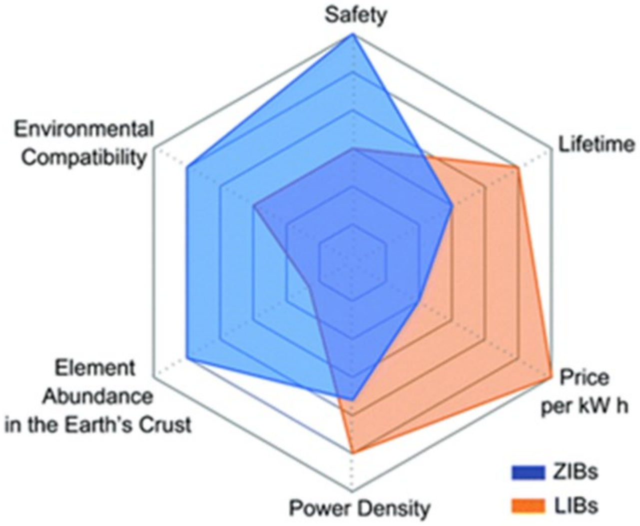

Figure 1.4 . Comparative analysis of zinc-ion and lithium-ion batteries from multiple perspectives.[16]

However, these materials' progress and widespread use have been limited by the absence of suitable cathode materials because of their low capacity and weak stability during charge-discharge cycles.[18] The increased polarity of the Zn^{+2} ion enables stronger electrostatic interactions with the cathode compared to monovalent cations such as Li^+, leading to a significantly reduced diffusion rate. Additionally, the energy density of ZIBs is constrained by the narrow working voltage window caused by the reduction potential of water. Hence, it is crucial to create an appropriate cathode substance that can efficiently and reversibly accept Zn^{+2} ions, has an enhanced ability to store electrical charge, and has a prolonged lifespan to progress ZIBs. Thus far, researchers have investigated various categories of inorganic cathode materials for their application in ZIBs. Nevertheless, these materials have faced obstacles such as a progressive decline in capacity and instability during cycling. Reasons for these obstacles are volume fluctuations, dissolving in the electrolyte, and phase transition problems. Furthermore, there are other problems for inorganic cathode materials. Inorganic units are toxic and can cause environmental pollution. Considering all these, the use of inorganic units as cathode materials in ZIBs has not become widespread. Molecules with redox-active groups have recently attracted attention as cathode materials in ZIBs because of their lightweight, eco-friendliness, affordability, and capacity to be adjusted at the molecular level. Molecules containing carbonyl and imine groups exhibited high redox activity compared to other functional groups.[19] However, there are some problems with using small organic molecules as cathode materials in ZIBs. For example, leaching of organic units into the electrolyte solutions during discharge, low conductivity, and cycling stability. Unfortunately, these problems have limited the use of these molecules in practical applications.[20]

1.2.2.1. Energy Storage Mechanism of Zinc-Ion Batteries

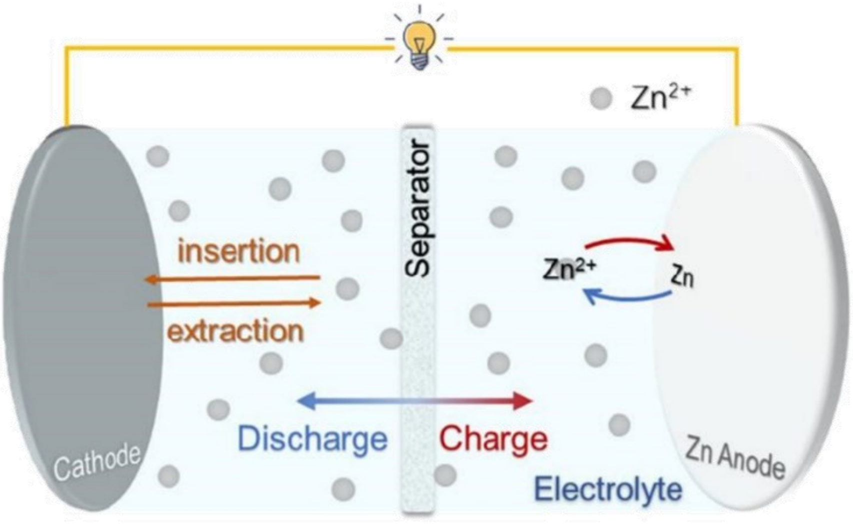

Figure 1.5. The working mechanism of Zinc-ion battery cell.[21]

The reversible insertion and extraction of Zn^{2+} in the host materials is the primary energy storage process, resembling that of regular Li-ion batteries. During discharge, the zinc metal anode undergoes dissolution, forming Zn ions in the electrolyte. The zinc ions are absorbed in the cathode. The electrolyte functions as a channel for the movement of ions. During the charging process, the reverse occurs. The cathode releases electrons, causing zinc ions to flow back to the anode as Zn^{2+} ions through the electrolyte. Zinc has a significant energy density, enabling it to store many charges despite having a tiny quantity of active material. No starting cycle is required for the formation of ZIB complexes. It is simple to use. Its popularity stems from its inherent risk-free nature.

Anode Reaction :

$$\mathrm{Zn} \leftrightarrow \mathrm{Zn}^{2+} + 2\mathrm{e}^{-}$$

Cathode Reaction :

$$\mathrm{M} + x\mathrm{Zn}^{2+} + 2x\mathrm{e}^{-} \leftrightarrow \mathrm{Zn}_x\mathrm{M}$$

Overall Reaction :

$$x\mathrm{Zn} + \mathrm{M} \leftrightarrow \mathrm{Zn}_x\mathrm{M}$$

Figure 1. 6. Universal equations for electron transfer in ZIB.[22]

At the anode, oxidation occurs to the zinc metal (Zn). During the discharge cycle, zinc undergoes oxidation and is transformed into zinc ions (Zn^{2+}) while simultaneously releasing two electrons ($2e^{-}$). At the cathode, the positive electrode, the material M, which can be any substance capable of intercalating zinc ions, such as manganese dioxide, reacts with zinc ions and electrons from the anode. Here, x denotes the stoichiometry, which is the ratio of zinc ions mixed with the cathode material. During the discharge process, the cathode material undergoes a reaction where it takes in zinc ions and electrons, resulting in the formation of a zinc compound known as Zn_xM.

1.3. Developments of Cathode Materials For Zinc-Ion Batteries

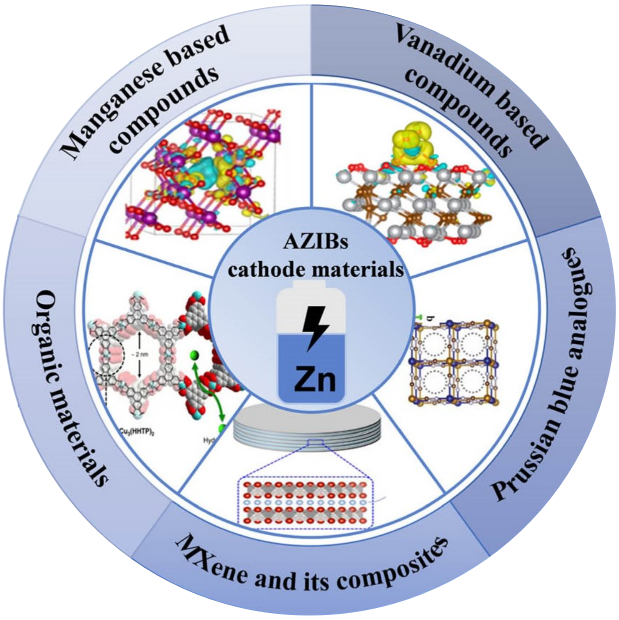

Figure 1.7. Cathode Materials for rechargeable aqueous zinc-ion batteries (AZIBs).[18]

While ZIB technology has rapidly advanced, it still faces limited energy density and short cycling life challenges. These challenges currently limit the practical use of ZIBs. The cathode electrode material plays a crucial role in ZIBs, acting as a host for Zn^{2+} (de)intercalation. It significantly influences the overall electrochemical performance of

ZIBs in aqueous systems. Due to the embedding and removal of ions during the charging and discharging operations, cathode materials should possess an initial open lattice structure and sufficient lattice stability to accommodate variations in lattice volume and potential complicated structural alterations. The primary cathode materials documented thus far include manganese-based compounds, vanadium-based compounds, PBAs, MXene, and certain organic materials.[18]

1.3.1. Manganese-based compounds

Manganese (Mn) is plentiful in the earth's crust, and materials containing manganese have been important in advancing AZIBs.[23] This material is abundant and easily accessible, relatively inexpensive, and environmentally sustainable, making it suitable for various uses in large-scale energy storage. Although manganese-based materials are widely utilized, challenges are still encountered during the charging and discharging procedures. At first, MnO_2 with various crystal types is susceptible to undergoing structural transformation, which results in the degradation of the crystal structure and subsequently causes a decrease in capacity over the battery cycle.[24] Moreover, the dissolution of Mn^{2+} and the formation of irreversible by-products are crucial obstacles that hinder the progress of manganese-based compounds as cathode materials for AZIBs.[25]

1.3.2. Vanadium-based compounds

Vanadium-based material is a highly effective cathode material for AZIBs. This is characteristic of plentiful reservoirs of resources, varied structures, and multiple valence states (V^{2+}, V^{3+}, V^{4+}, and V^{5+}). Vanadium-based materials in polyvalent states can undergo multistep redox reactions, resulting in a high theoretical specific capacity of over 300 mA h g^{-1}.[26] Vanadium-based materials typically consist of interconnected V–O polyhedra. Despite the potential applications of vanadium-based oxides, the persistent issue of vanadium dissolution is a significant challenge in achieving consistent performance in AZIBs.

1.3.3. Prussian blue and Prussian blue Analogs (PBAs)

Aside from the conventional manganese and vanadium-based compounds, PBAs have been explicitly generated for application in the cathode of AZIBs.[27] Prussian blue, and PBAs might be jointly called metal-iron cyanides or metal hexacyanoferrates. PBAs can be produced by substituting Fe^{2+} and Fe^{3+} in the Prussian blue material with other transition metal ions. PBAs have a high working voltage platform of approximately 1.5-1.8 V, so they exhibit excellent ionic conductivity and the ability to charge and discharge rapidly.[28] While this material has a relatively low specific capacity of less than 200 mA h g^{-1}, its low cost, environmental friendliness, and straightforward synthesis make it a promising option for ZIB cathode materials. Nevertheless, their capacity is restricted, and their cyclic stability is inadequate due to the absence of redox sites and structural damage caused by ion dissociation.

1.3.4. MXene

MXenes are two-dimensional (2D) materials made from transition metals, carbides, or nitrides. MXenes exhibit remarkable compositional diversity and tunable properties due to their diverse chemical elements and unique layered structure. These features of MXenes provide remarkable attributes like high electrical conductivity and outstanding mechanical characteristics, making them highly valuable for various applications, including energy storage.[29] However, due to their limited voltage and capacity, MXenes can not be used alone. Instead, they are utilized along with other active materials in AZIBs. MXenes, as cathode materials in zinc ion batteries, may have several disadvantages, including a limited specific capacity and the possibility of degradation over extended cycling. In addition, the susceptibility of MXenes to oxidation in moist and oxygen-rich conditions may present difficulties with maintaining consistent battery performance.

1.3.5 Redox Active Organic Materials

Compared to other materials used as cathode materials in ZIBs, organic materials are more valued due to their environmental friendliness, economical nature, and tunable structure.[30] The organic cathode materials do not contain heavy metals. It can be produced by using sustainable resources and reaction pathways. By modifying the structure of organic materials, various electrochemical properties of organic materials could be customized, such as specific capacity, potential, electrical conductivity, solubility, and mechanical qualities. Organic materials with abundant electroactive sites in their structures typically show rapid reaction kinetics. For instance, C═O, ═NH$^+$, and C═N may act as storage sites for Zn^{2+} with redox-activity. Various organic cathode materials have been developed for ZIBs, including small organic molecules containing carbonyl or amino groups, polyaniline, porous organic polymers like COFs, and other conductive polymers.

1.3.5.1 Small Organic Molecules

Organic compounds offer greater flexibility in molecular design, enabling precise manipulation of voltage, capacity, conductivity, redox kinetics, and other properties essential for electrode materials. The carbonyl group-containing compounds with a small molecular weight have the potential to offer a high theoretical capacity for the material.

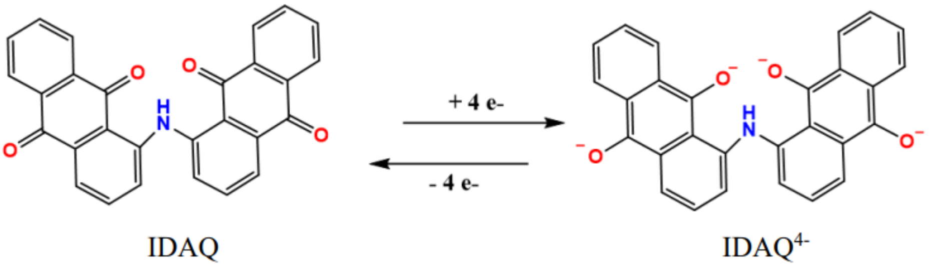

Figure 1.8. The electrochemical reaction during charging and discharging.[31]

Due to their high redox properties and stable structure, quinone-based small organic molecules can serve as cathode materials in ZIBs. As shown in Figure 1.8, Zn^{2+} storage in quinone-based compounds occurs when a positively charged ion at the cathode binds to a negatively charged oxygen atom (C-O$^-$). At the same time, a carbonyl group (C=O) undergoes reduction. Another functional group present in the molecules used as cathode materials in zinc ion batteries is the imine group. Molecules containing imine groups can be used as cathode materials in zinc ion batteries because of their beneficial properties, such as high energy storage capacity and redox activity. The active functional group of imine compounds (C=N) can receive electrons during discharge and transform into (-C-N$^-$) anions, while the charge balance is maintained by the entry of cations (Zn^{2+} or H^+). Moreover, the presence of N atoms can enhance electron conduction and increase the redox potential. Additionally, recent research shows that organic molecules containing multiple redox-active groups achieve high energy density. Recently, molecules containing dual redox groups, C=O and C=N, have been used as cathode materials ZIBs.

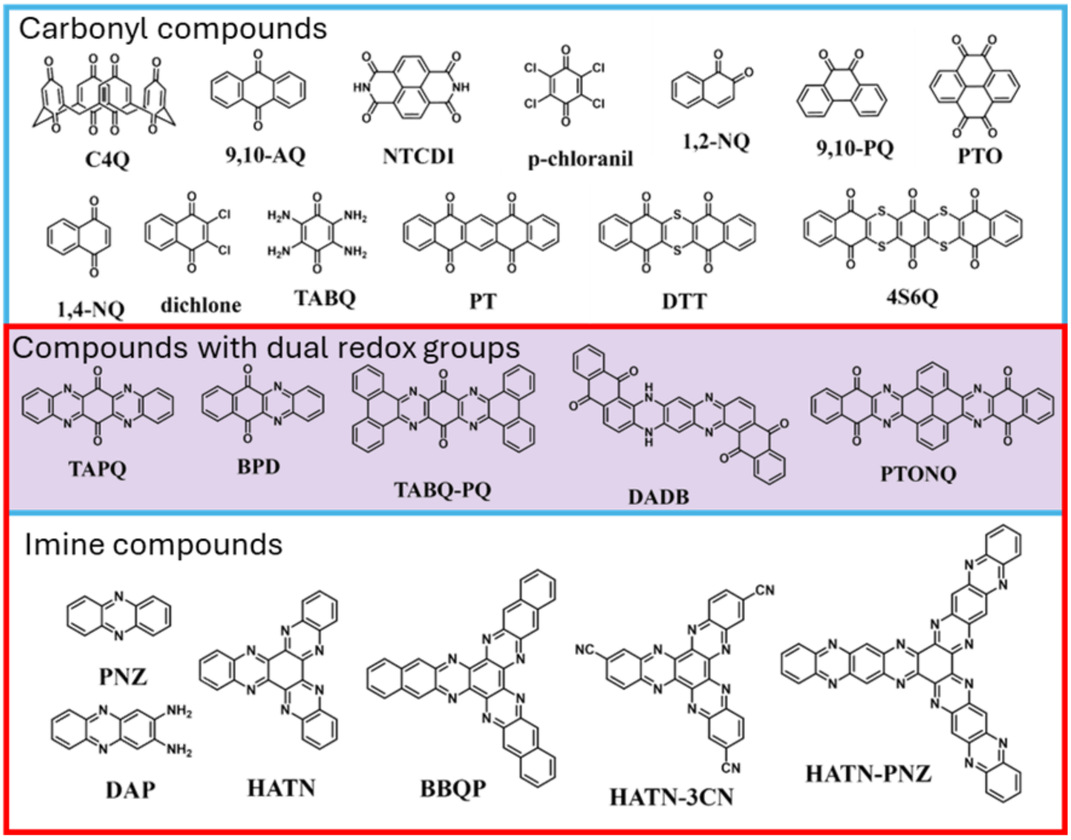

Figure 1.9. Structures of common small organic molecules used as cathode materials in ZIBs. ((C4Q)[32], (9,10-AQ)[32], (1,2-NQ)[32], (9,10-PQ)[32], (TABQ)[33], (1,4-NQ)[32], (dichlone)[34], (p-chloranil)[35], (PTO)[36], (NTCDI)[37], (PT)[38], (DTT)[39], (4S6Q)[40], (TAPQ)[41], (BPD)[42], (TABQ-PQ)[43], (DADB)[44], (PTONQ)[45], (PNZ)[46], (DAP)[47], (HATN)[48], (BBQP)[49], (HATN-3CN)[50], (HATN-PNZ)[51].

1.3.5.2 Polyaniline (PANI)

The accessibility of raw materials, simple synthesis process, excellent stability, and diverse structure attract significant interest to PANI for ZIBs. Nevertheless, the inherent nature of PANI does not have conductivity. Only when acid is added can it work as a cathode in ZIBs.[52] However, zinc will undergo corrosion in acidic environments. Therefore, picking the right way to add doping is essential to find a balance between protecting the zinc anode from corrosion and keeping the high electrochemical activity of PANI. There are two main ways to dope PANI. The first one is called self-doping PANI. It bonds to a particular framework and becomes a polymer without much extra help. In 1985, Macdiarmid and colleagues created hydrochloric acid-doped PANI on graphite electrodes to use as anode material in ZIBs. Their research investigated how effective hydrochloric acid doping was, and they found that the battery they made could be charged and discharged repeatedly using a $ZnCl_2/NH_4Cl$ electrolyte. Another way to dope PANI is through copolymerization. The substance mixed with aniline during polymerization needs to do two things in this method. First, it should be able to provide protons. Second, it should help reduce the amount of inactive stuff and increase the battery's theoretical capacity. Sun and colleagues showed how to make a sulfo-self-doped PANI cathode for rechargeable aqueous ZIBs. They used aniline and methanolic acid copolymer to construct an organic cathode for aqueous ZIBs. The sulfuric acid part in benzene sulfonic acid, which acts as a self-dopant, helps keep a high concentration of H^+ ions close to the PANI cathode, which makes the cathode work well for storing and releasing energy.

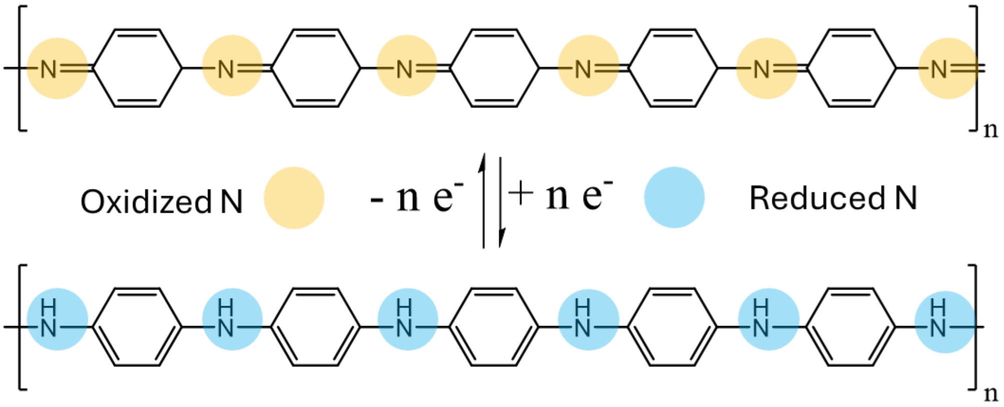

Figure 1.10. Energy storage mechanism of PANI

1.3.5.3 Porous Organic Polymers (POPs)

Porous organic polymers (POPs), which are porous materials, are synthesized by covalently bonding organic compounds to form polymeric networks. These materials include unique chemical and physical characteristics, such as significant surface area, adjustable pore size, and exceptional physical and chemical stability.[53] Unlike discrete organic compounds, POPs do not have dissolution problems. This feature dramatically decreases the chance of substances leaking into the electrolyte solution during battery operation. Each of these properties makes POPs highly suitable as cathode materials for ZIBs.[54] In addition, their easily tunable structures at the molecular level have made them essential candidates for not just energy storage but also for areas such as CO_2 capture,[55] hydrogen evolution,[56] and chemical sensing.[57]

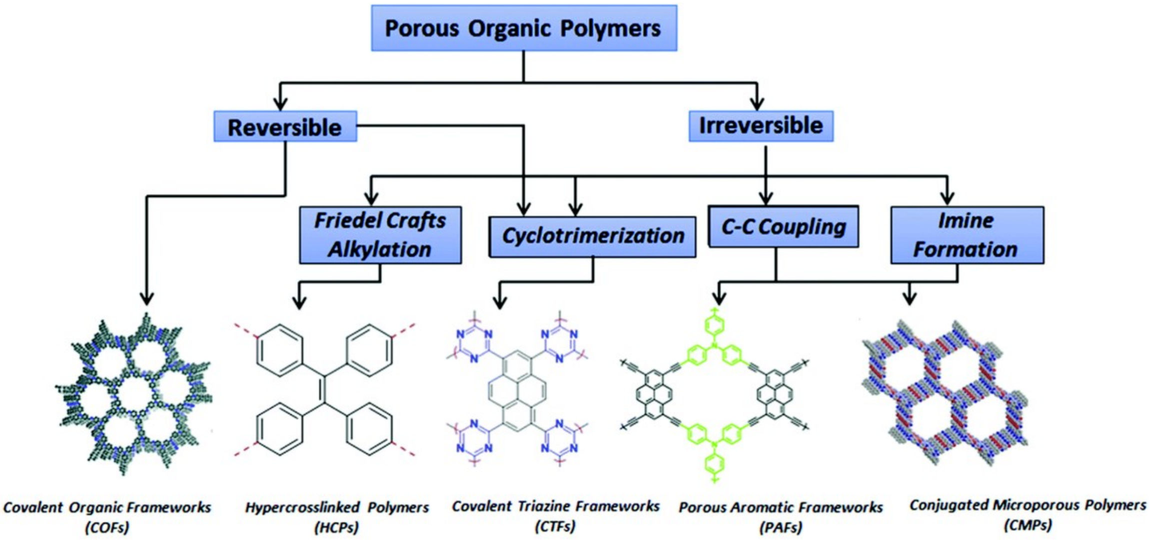

Figure 1.11. Schematic illustration of types of porous organic polymer frameworks and their formation reactions.[58]

POPs can be divided into five groups depending on their synthesis methods and structures. These are porous aromatic frameworks (PAFs), covalent triazine frameworks (CTFs), covalent organic frameworks (COFs), hypercrosslinked polymers (HCPs), and conjugated microporous polymers (CMPs). Except for some examples like CTFs and COFs, which have precisely ordered structures formed under specific thermodynamic conditions, most porous organic polymers (POPs) are amorphous.[58]

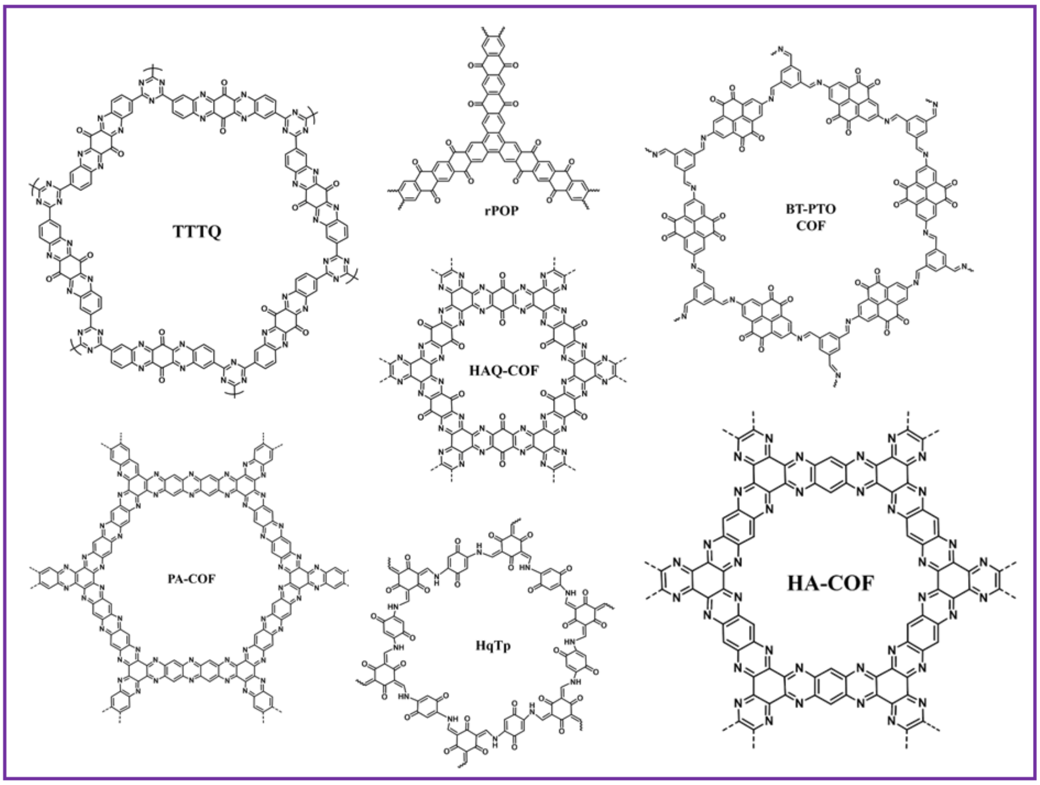

Figure 1.12. Structures of porous organic polymers used as cathode materials in ZIBs. ((TTTQ)[59], (rPOP)[60], (BT-PTO COF)[61], (HAQ-COF)[62], (HA-COF)[62], (HqTp)[63], (PA-COF)[64]).

Many porous organic polymers have previously been tried as cathode materials in ZIBs. Some of the POPs that have been tried before are listed above (Figure 1.12). POPs have demonstrated good electrochemical performance in capacity and rate. However, these polymers still have challenges to address. These challenges, such as the requirement for specific additives because of their limited lifespan, limited conductivity, and consistent discharge plateau for stable voltage output, all of which hinder their practical use. Therefore, developing new electrochemically active POPs and comprehending their Zn^{2+} storage mechanism remains crucial to achieving the desired electrochemical performance and cost advantages.

1.3.5.4 Conjugated Polymers

Apart from small organic molecules, PANI, and POPs, conjugated polymers (CPs) are another materials used as cathode materials in ZIBs. Conjugated polymers with an expanded π-conjugated system enhance π-electron delocalization, lower the total energy gap between HOMO and LUMO levels, and significantly speed up the transfer of intramolecular electrons during charging and discharging. Additionally, the planar conjugation system can improve the diffusion kinetics of zinc ions. Furthermore, CPs have become a promising choice for cathode materials in ZIBs due to their easy synthesis through conventional methods like oxidative polymerization, electropolymerization, and copolymerization, along with their ability to be chemically modified to meet different requirements.

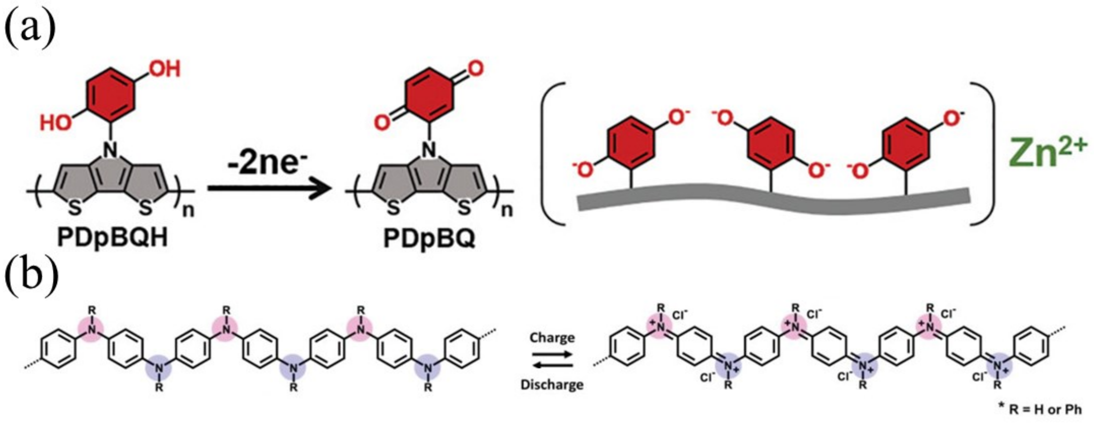

Figure 1.13. (a) Schematic of o polymers PDpBQH was oxidized to work in ZIBs.[65] (b) Redox mechanism of m-PTPA.[66]

The figure above illustrates the proposed redox mechanisms of the two conjugated polymers in ZIBs. In 2021, Wang and coworkers synthesized hydroquinone-twisted PDpBQ for high-performance and durable ZIBs. PDpBQ exhibited rapid charge transfer and excellent redox reaction reversibility due to its good molecular planarity and uniform electrostatic potential (ESP) distribution, which benefit Zn^{2+} hosting (Figure 1.13a). In a 2021 study, Zhang and colleagues developed a redox-active m-PTPA. The redox mechanism of m-PTPA is shown in Figure 1.13b. The benzene ring changes to a quinoid ring during the charging process, and the amine groups become positively charged amine and imine groups. These positively charged groups interact with Cl^- anions to form N–Cl^- chemical bonds.

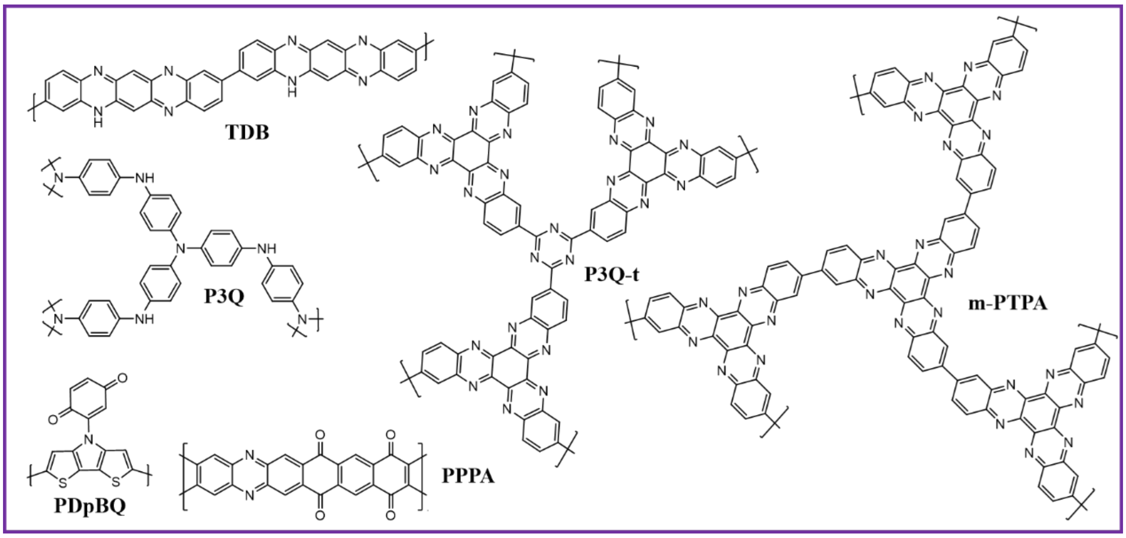

Figure 1.14. Structures of conjugated polymers used as cathode materials in ZIBs. ((TDB)[67], (P3Q)[68], (PDpBQ)[65], (PPPA)[69], (P3Q-t)[68], (m-PTPA)[66]).

Figure 1.14 shows various examples of conjugated polymers employed as cathode materials in ZIBs. These example conjugated polymers share several similar characteristics. One of these critical features is a flexible structure. Unlike inorganic cathodes, the flexible structure can offer elastic matrices for Zn^{2+} storage, preventing lattice expansion, shrinkage, and structural strain. Also, the flexible structure of CPs can endure mechanical stress, which helps maintain structural integrity during repeated cycling. The conjugated chemical bonds enable them to retain cations while discharged. CPs can further enhance their conductivity by doping the conjugated polymer with ions. Additionally, these conducting polymers' theoretical specific charge values are comparable to those of inorganic metal oxide electrodes. This similarity raises expectations for the acceptable electrochemical performance of conducting polymer cathodes in ZIBs Although these polymers are promising for ZIBs, their electrochemical performance in capacity, rate capability, and cyclability still falls short of expectations.

1.4 Literature Studies

In 2020, Wang and colleagues prepared MnO_2 and D-MnO_2 nanowires as cathode material.[70] In this study, a thin structure with a diameter of about 10 nanometers was obtained using a solvation method. As shown in Figure 1.15(a), these nanowires exhibited abundant oxygen vacancies and lattice holes Surprisingly, cathode material D-MnO_2

performs significantly better than its defect-free MnO$_2$ counterpart. It demonstrates a high energy density of 406 W h kg^{-1}, proper rate capability, and exclusive stability over 1000 cycles. The rate performance of the cathodes is compared in Figure 1.15(b). The D-MnO$_2$ cathode achieves a high initial specific capacity of 290 mA h g^{-1} at a current density of 0.3 A g^{-1}, compared to MnO$_2$. Even as the current density increases to 3.0 A g^{-1}, the specific capacity remains at 134 mA h g^{-1}, demonstrating proper rate capability. Also, D-MnO$_2$ shows more extended cycling stability. Figure 1.15(c) illustrates the cycling performance of both cells at the current density of 0.6 A g^{-1}. The D-MnO$_2$ cell has an increased initial specific capacity of 263 mA h g^{-1}, with an identical Coulombic efficiency of 91.9%. This study is significant for developing MnO$_2$ materials for ZIBs with high energy density and long cycleability.

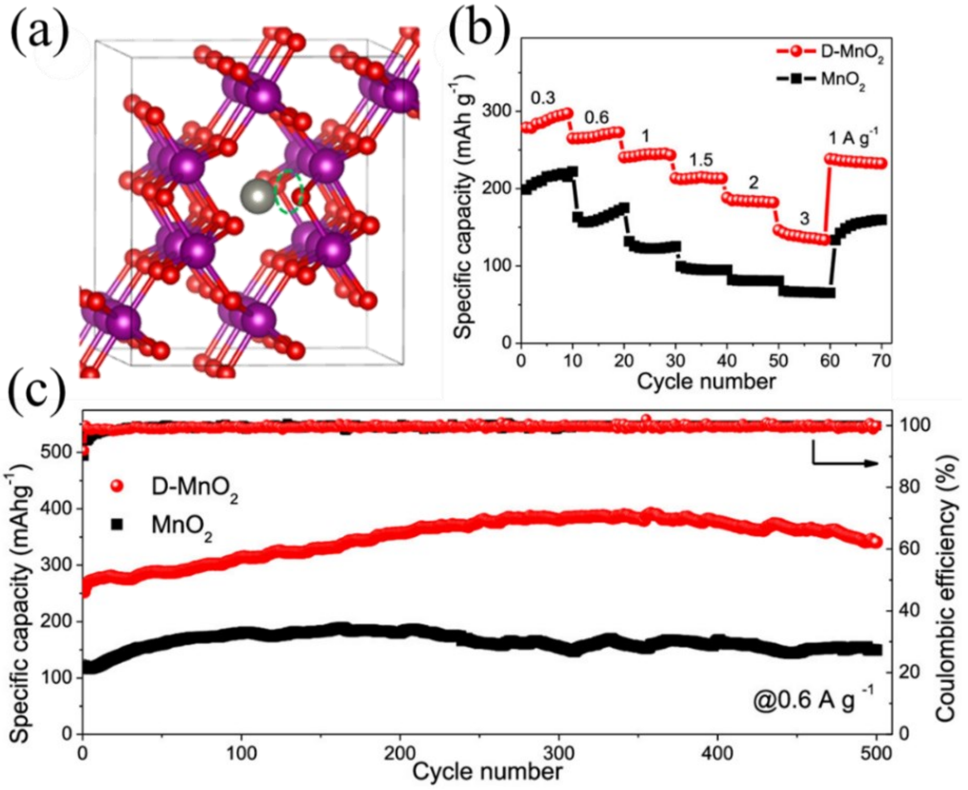

Figure 1.15. (a) Adsorption structure of Zn in D-MnO$_2$, (b) rate capability of D-MnO$_2$, (c) cycling stability of the D-MnO$_2$ and MnO$_2$ cathodes.[70]

Another example is a study using a small organic molecule as a cathode material. In this study reported by Zhao et al. in 2018, quinone-based organic molecules were used as the electrode material in ZIBs.[32] They investigated different quinone-based molecules with carbonyl groups in the para-position [1,4-naphthoquinone (1,4-NQ), 9,10-anthraquinone (9,10-AQ), and calix[4]quinone (C4Q)] and ortho-position [1,2-

naphthoquinone (1,2-NQ) and 9,10-phenanthrenequinone (9,10-PQ)] as cathodes in aqueous ZIBs (Figure 1.16(a)). Figure 1.16(b) shows that the capacity retention of the Zn-C4Q batteries is 93% after 100 cycles. The evolution of morphology indicates that the Zn anode is protected without forming side products. Also, Figure 1.16(c) demonstrates that after 1000 cycles at 500 mA g^{-1}, the capacity retention remains at 87%, decreasing by only 0.015% per cycle. Figure 1.16(d) demonstrates that quinone-based compounds with carbonyl groups (C=O double bonds) in the para-position (1,4-NQ, 9,10-AQ, and C4Q) generally exhibit higher capacity and a smaller gap between charge and discharge compared to those with carbonyl groups in the ortho-position (1,2-NQ and 9,10-PQ).

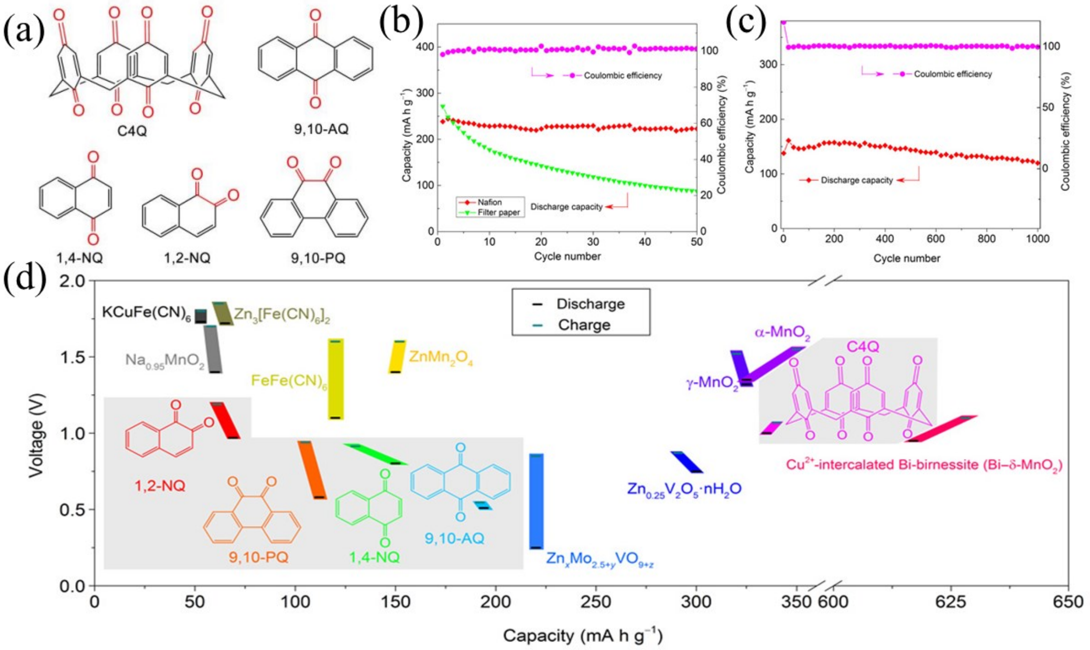

Figure 1.16. (a) Structures of the quinone-based organic molecules. (b) cycling performance of Zn-C4Q batteries at a current density of 100 mA g^{-1}, (c) cycling performance of Zn-C4Q batteries at a current density of 500 mA g^{-1}, (d) discharge/charge voltages of quinone base molecules.[32]

In a study conducted by Zheng Li and coworkers in 2022, the synthesized conjugated microporous polymer was used as a cathode material in ZIBs, and the charge storage mechanism of the battery was examined.[71] Figure 1.17 shows how G-Aza-CMP was synthesized. First, hexaketocyclohexane octahydrate and 1,2,4,5-tetraaminobenzene tetrahydrochloride were mixed in solvothermal condensation reaction conditions to yield the Aza-CMP material. Next, the Aza-CMP was mixed into a graphene oxide water solution and then processed using hydrothermal to form the G-Aza-CMP composite. To verify the synthesized structure, various characterization analyses such as FT-IR, ^{13}C solid-state NMR, XRD, SEM, TEM, and BET were conducted.

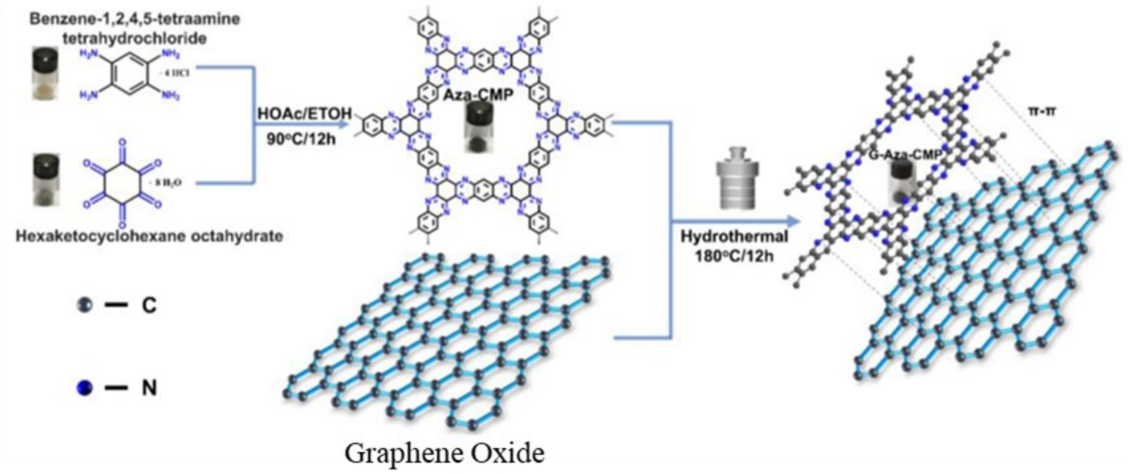

Figure 1.17. Synthetic pathways for Aza-CMP and G-Aza-CMP.[71]

Figure 1.18(a) demonstrates that the cathode G-Aza-CMP provides a strong discharge capacity of 456 mAh g^{-1}, which is 76% of its theoretical capacity of 602 mAh g^{-1}, at a current density of 0.05 A g^{-1}. Figure 1.18(b) indicates the capacities obtained at different current densities. The G-Aza-CMP electrode achieved discharge capacities of 398, 345, 300, 265, 259, 225, and 200 mAh g^{-1} at current densities of 0.1, 0.2, 0.5, 1.0, 2.0, 5.0, and 10.0 A g^{-1}, respectively. When examining the cyclic voltammetry analysis, four redox peaks are observed in the G-Aza-CMP electrode at approximately 0.64V, 0.42V, 0.99V, and 0.81V, as shown in Figure 1.18(c). According to Figure 1.18(d), the cycling performance of the G-Aza-CMP electrode was initially evaluated at a low current density of 0.1 A g^{-1}. After 100 cycles, the capacity retention was found to be 85.0% of the initial capacity. Also, when the current density was increased to 1.0 A g^{-1}, the battery retained 91.7% of its initial capacity after 1000 cycles. In addition, the G-Aza-CMP electrode exhibited long-term durability, with only an 8.3% decrease in capacity over 9700 cycles at a current density of 10 A g^{-1} (Figure 1.18(e)).

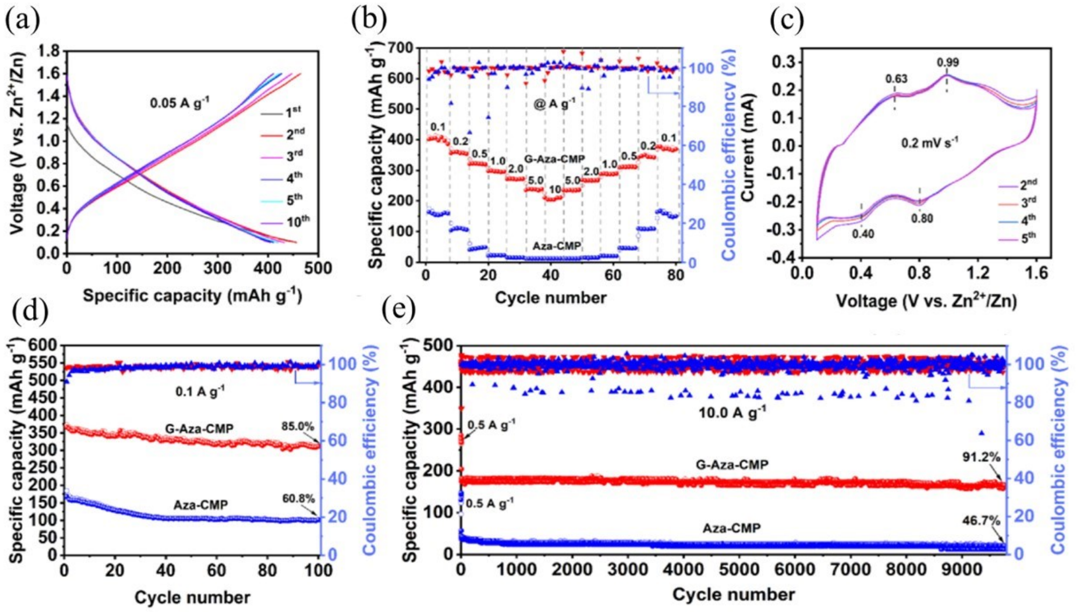

Figure 1.18. (a) Galvanostatic CD measurements of G-Aza-CMP (b) rate capability test of G-Aza-CMP and Aza-CMP, (c) Cyclic voltammetry measurements of G-Aza-CMP, Long term cycling stability tests for G-Aza-CMP and Aza-CMP cathodes at a current density of (d) 0.1 A g^{-1} and (e) 10.0 A g^{-1}.[71]

The same study used different physical and chemical methods to analyze how G-Aza-CMP stores charge in zinc-ion batteries (ZIBs). The C=N functional groups in G-Aza-CMP, shown in Figure 1.19(a), act as reactive sites that can coordinate with different amounts of Zn^{2+} and H^{+}. To verify this coordination, a method called electrostatic potential surface (EPS) was exhibited. As shown in Figure 1.19(b), the C=N functional groups are primarily located in the blue region, which has a negative ESP value. Ex-situ characterizations were performed at different stages, as shown in Figure 1.19(c). FT-IR spectra revealed that the peaks at 1233 cm^{-1} for C=N in the aza ring gradually disappear during discharge and reappear during charge (Figure 1.19(d)). In Figure 1.19(e), X-ray photoelectron spectroscopy (XPS) analysis was used to examine the N, S, and Zn states in the cathode at different stages. Additionally, as shown in Figure 1.19(f), the zinc hydroxide sulfate composition on the cathode surface at different discharge stages was confirmed using ex-situ XRD.

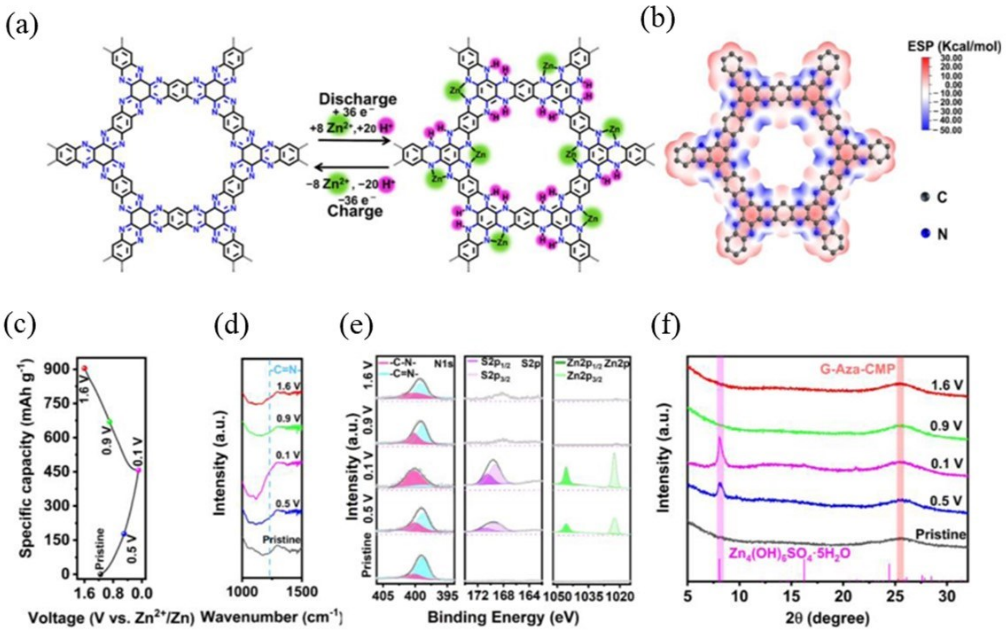

Figure 1.19. (a) Charge storage mechanism for G-Aza-CMP. (b) Electronegativity simulation of Aza-CMP. (c) Galvonastatic CD curve for the first cycle at a current density of 0.05 A g^{-1}. Ex-situ analysis: (d) FT-IR. (e) XPS (f) XRD.[71]

Another cathode example was developed by Weihua Tang and his colleagues in 2021. In 2022, Tang and their team made two triquinoxalinylene (3Q) polymers.[68] The names of these polymers are homopolymer (P3Q) and triazine-linked 3Q polymer (P3Q-t), and two different procedures are used for each polymer. The procedure of synthesis P3Q adopted solvent-free polymerization while the procedure of P3Q-t was a two-step reaction; the first step was Knoevenagel condensation, and the second step was a trimerization reaction catalyzed by anhydrous zinc chloride. This study shows the effect of the planarity of polymers on electrochemical performances.

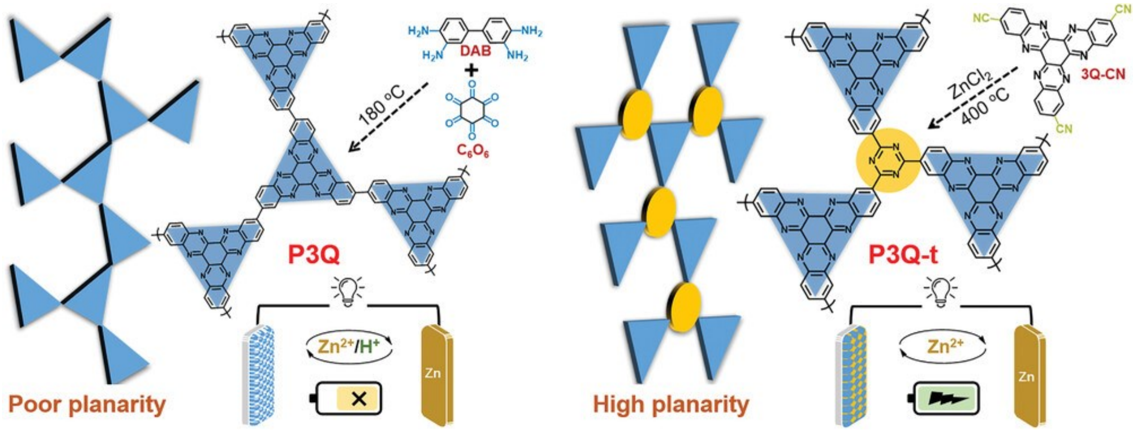

Figure 1.20. Synthesis of P3Q and P3Q-t.[68]

To investigate the electrochemical capabilities of P3Q and P3Q-t cathodes, a Zn foil anode and a 2 M $ZnSO_4$ electrolyte were employed. CV tests were exhibited to investigate the reversibility of the redox reactions for the battery containing P3Q and P3Q-t. CV measurements were recorded between 1−5 mV s^{-1} scan rates (Figure 1.21 (a)). As a result of the CV measurements, two oxidation peaks at 0.63 V and 1.1 V and two reduction peaks at 0.32 V and 1.0 V were observed for P3Q. For P3Q-t, at the end of this measurement, one oxidation peak at 0.63 V and one reduction peak at 0.32 V were observed. Furthermore, *b*-values for each polymer were calculated to investigate the relationship between scan rates (*v*) and current (*i*) in the CV (Figure 1.21 (b)). The results show that P3Q has slower and more unstable ion diffusion than P3Q-t. Galvanostatic charge-discharge (GCD) measurements were conducted to analyze the capacity of each P3Q and P3Q-t battery. As a result of these measurements, P3Q showed just 115 mA h g^{-1} capacity at a current density of 0.3 A g^{-1}, while P3Q-t exhibited 237 mA h g^{-1} capacity at the same current density (Figure 1.21 (c)). Also, both polymers achieved excellent Coulombic efficiency of 100%. Long-term cycling stability tests were conducted to investigate the cycling stability of each cathode. P3Q-t showed a more successful result than P3Q. This result is a capacity retention rate of 81% at the end of 1500 cycles (Figure 1.21 (e)). Compared to other organic ZIB cathodes in the literature, P3Q-t achieved acceptable electrochemical results (Figure 1.21 (d)).

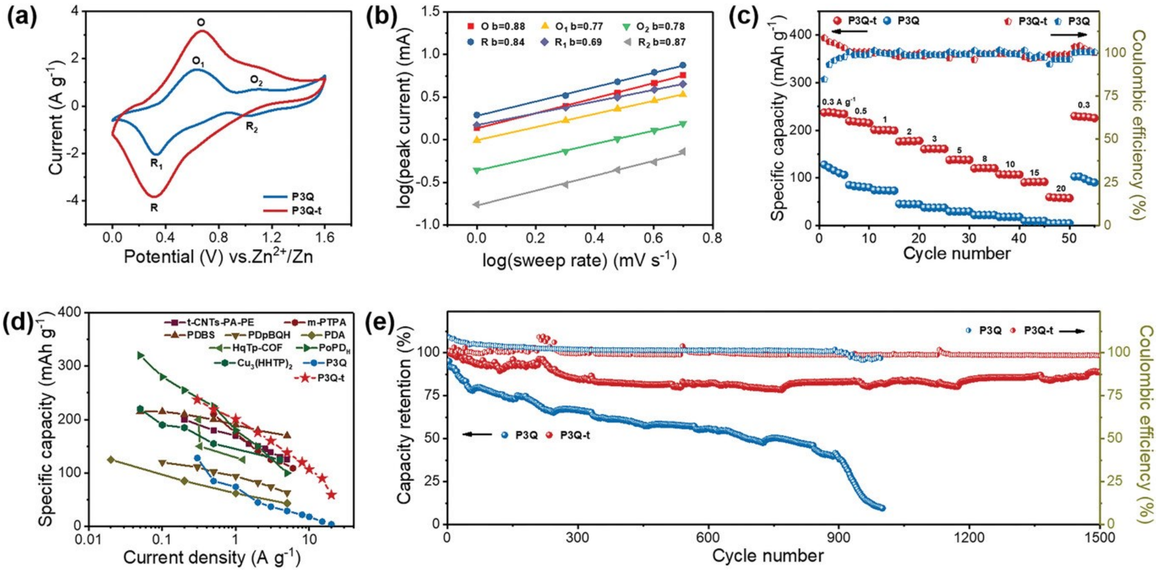

Figure 1.21. (a) Cyclic Voltammetry results at 5 mV s^{-1}. (b) b-values for each oxidation and reduction peaks. (c) Rate performance of P3Q and P3Q-t cathodes. (d) Specific capacity results compare to other organic cathode examples. (e)Long-term cycling stability test for P3Q and P3Q-t.[68]

The co-insertion of H^+ and Zn^{2+} ions was studied to understand how the P3Q and P3Q-t electrodes store charge. To understand charge storage mechanisms, ex-situ FT-IR and XPS analyses were carried out. The ex-situ FT-IR analysis verified the changes of C=N groups in both P3Q-t and P3Q (Figure 1.22(a)). Specifically, in the charged state, both electrodes exhibit pyrazine C=N peaks at 1500-1680 cm^{-1}, which decreases in intensity in the discharged state. Additional ex-situ XPS research provides further insights into the composition transition for the C, N, and Zn elements. Both polymer cathodes demonstrate redox reactions involving Zn^{2+}. According to the computation of the areas, it has been found that P3Q-t has a more significant migration of Zn^{2+} (65.7%) compared to P3Q (49.6%) (Figure 1.22 (b-d)). In addition, CV measurements with H_2SO_4 electrolyte were recorded to support the XPS results for co-insertion of H^+ and Zn^{2+} ions (Figure 1.22 (e-f)).

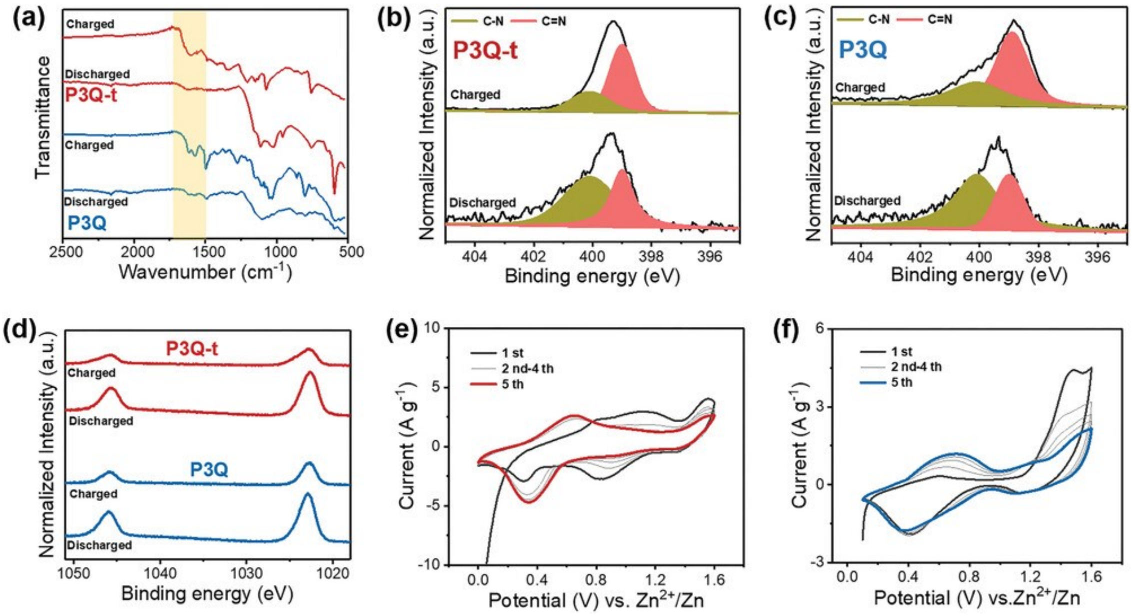

Figure 1.22. (a) Ex-situ FTIR analyses for both polymer at charged and discharged states. High-resolution XPS spectra for N 1s region (b) P3Q-t (c) P3Q. (d) Zn 2p region high-resolution XPS spectra for both polymers. Cyclic voltammetry results with H_2SO_4 electrolyte (e) P3Q-t (f) P3Q.[68]

Additionally, in a study conducted by the Linfeng Hu Research Group in 2022 using a quinone-based conjugated polymer, the electrochemical performances of the conjugated polymer in ZIBs were evaluated.[69] The name of the synthesized polymers is poly(phenazine-alt-pyromellitic anhydride) (PPPA), which was synthesized due to condensation polymerization. Figure 1.23(a) shows that a molar mixture of 2 $AlCl_3$ and 1 NaCl was infused at 160 °C to obtain the fused salt. Phenazine and PMDA were added to the fused salt and rotated at 250 °C for one day.

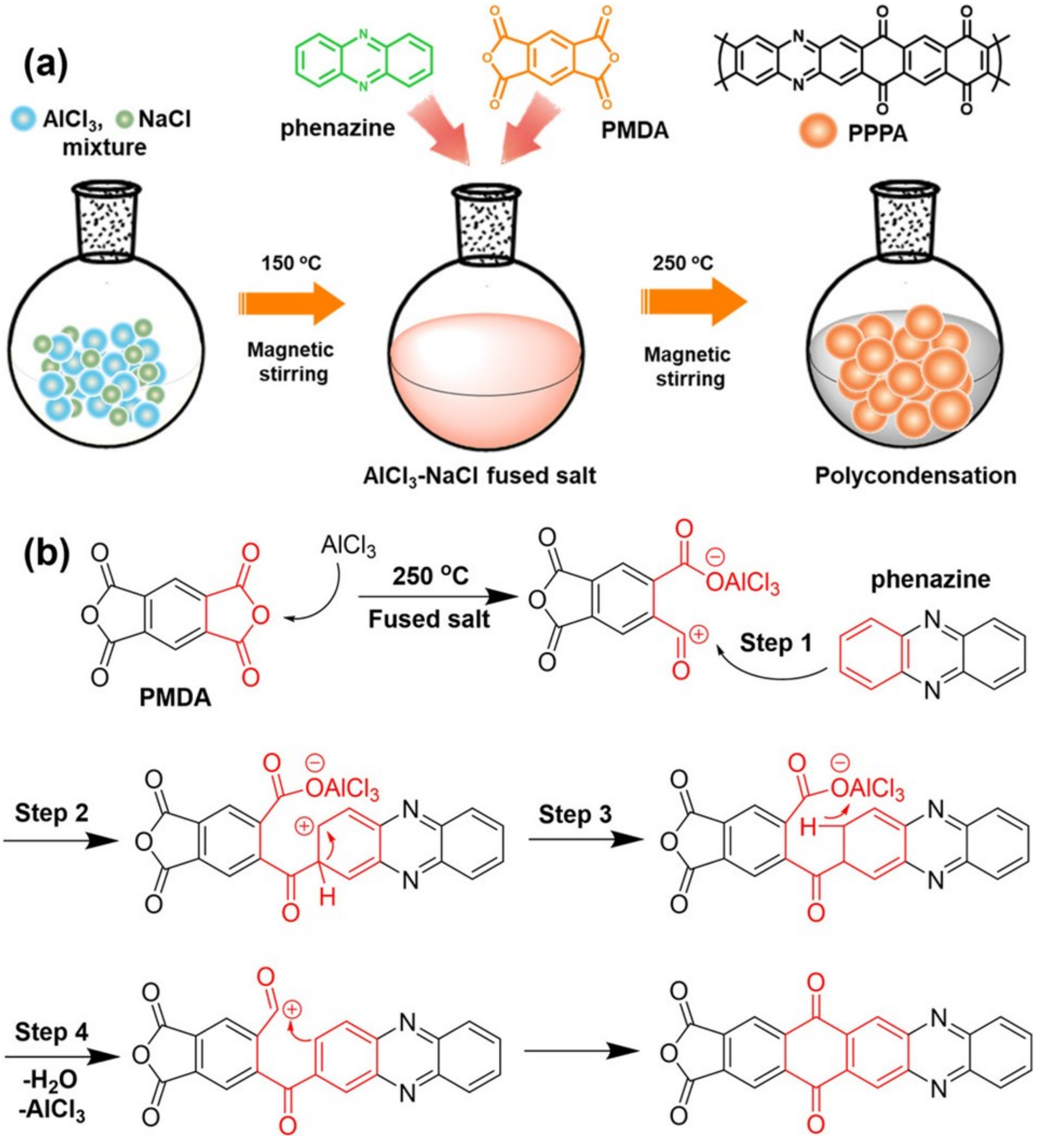

Figure 1.23. (a) Synthetic pathway for PPPA, (b)The mechanism of Friedel–Crafts reaction.[69]

The Friedel–Crafts reaction of PPPA, where phenazine reacts with pyromellitic anhydride, as shown in Figure 1.23(b). The novel polymer PPPA was analyzed using FT-IR, NMR, XRD, TEM, and Raman measurements. The characterized polymer was then tested for its electrochemical properties. CV analysis of PPPA, shown in Figure 1.24(a), revealed peaks at 0.56 V and 0.73 V. The Galvonastatic charge-discharge profiles of the PPPA cathode are characterized by sloped charge-discharge plateaus and stable capacities around 210 mAh g^{-1} from the 2nd to the 10th cycle at 50 mA g^{-1} (Figure 1.24(b)).

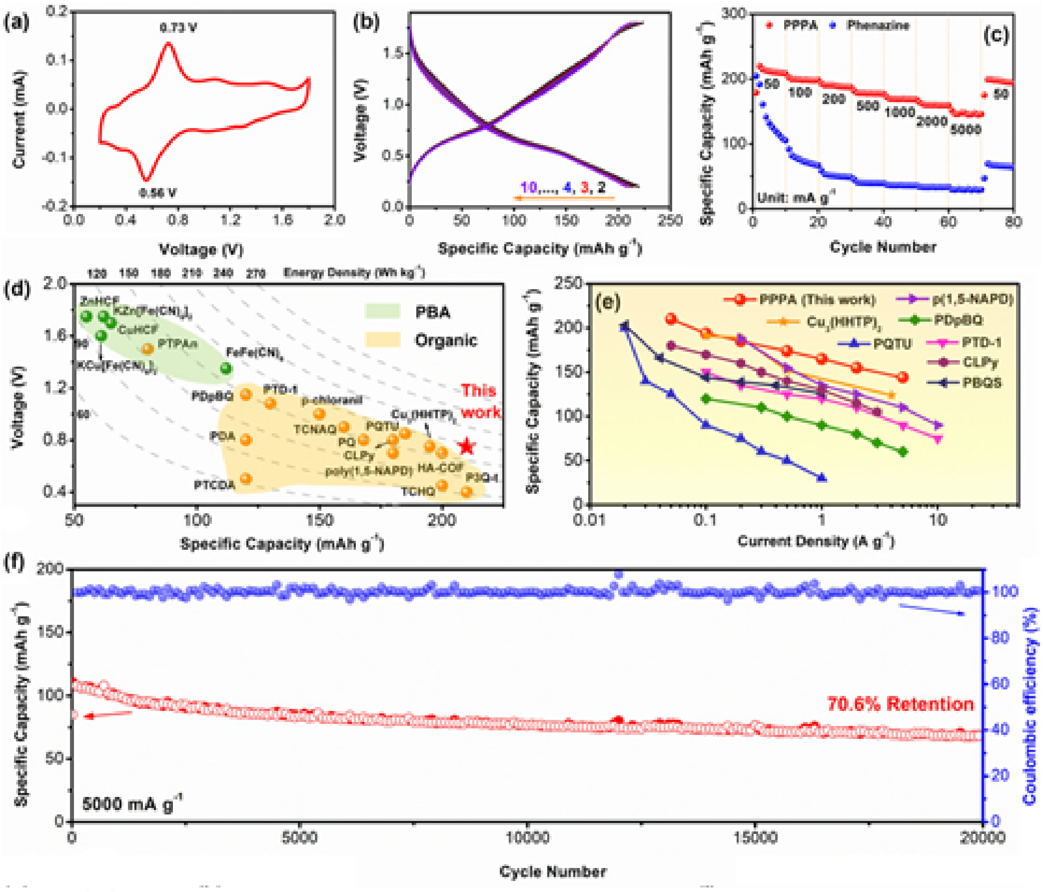

Figure 1.24. (a) Cyclic Voltammetry plot of PPPA, (b) Galvonastatic charge-discharge plot of PPPA, (c) Rate Performance of PPPA and phenazine, (d) Comparison of specific capacities between PPPA and previously reported conjugated polymer-based ZIBs, (e) Comparison of rate performance capacities between PPPA and previously reported conjugated polymer based ZIBs, (f) Long-term cycle performance of PPPA at 5000 mA g^{-1}.[69]

It is important to note that the PPPA cathode's electrochemical stability is better than the phenazine and PMDA monomers. This effect is likely due to the large π-conjugated structure, which helps increase electrochemical activity and improve redox reversibility. Figure 1.24(c) shows the rate performance of PPPA cathodes tested at different current densities. Specific capacities of PPPA obtained with current densities 50, 100, 200, 500, 1000, 2000, and 5000 mA g^{-1}, respectively, 210.2, 191, 182.1, 170.9, 162.3, 154.4, and 139.7 mAh g^{-1}. When the current density was converted back to 50 mA g^{-1}, a capacity of 190.6 mAh g^{-1} was obtained. As seen in Figure 1.24(d) and (e), when compared with other examples in the literature, a very effective electrochemical result was obtained in zinc ion batteries operated using conjugated polymers as cathode material. The initial capacity was 140.6 mAh g^{-1}, and it remained at 92 mAh g^{-1} after

20,000 cycles, achieving a capacity retention rate of 70.6% with nearly 100% Coulombic efficiency (Figure 1.24(f)).

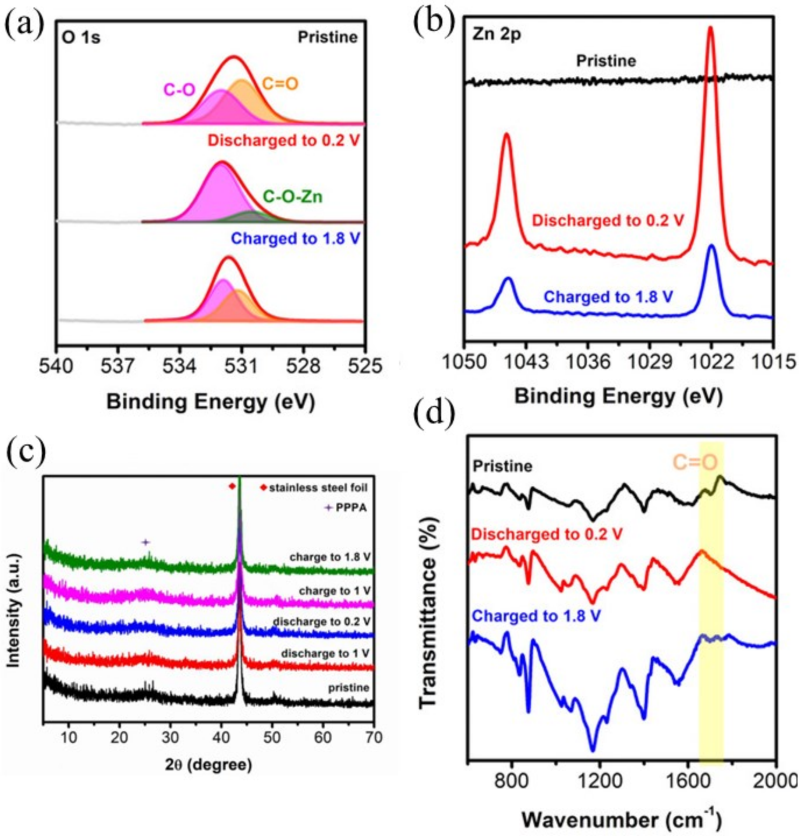

Figure 1.25. Ex-situ characterizations (a) and (b) XPS spectra, (c) XRD pattern, (d) FT-IR.[69]

The high-resolution O 1s XPS spectrum (Figure 1.25(a)) shows that the peak related to the C=O group (531 eV) disappeared after discharge, but the peak related to the C=O group returned at an intense level at charging. This indicates that there is a reversible transition between the C=O and C−O groups in the PPPA. Furthermore, in the fully discharged state, a new peak at 530.5 eV corresponding to C−O−Zn was seen (Figure 1.25(b)). This confirms that Zn^{2+} ions form coordination bonds with carbonyl groups in the polymer structure during discharge. In addition, the unique peak at 1710 cm^{-1}, which is associated with carbonyl groups, diminished when the battery was at a discharge state (0.2 V) and reappeared when it was fully charged (1.8 V). This shows that the carbonyl groups undergo a reversible enolization process (Figure 1.25(d)).

CHAPTER 2

EXPERIMENTAL STUDY

2.1 General Materials

The starting substances and solvents were acquired from Fluorochem, Sigma Aldrich, and Tokyo Chemical Industry (TCI) and were utilized without additional purification. The process of thin-layer chromatography (TLC) was carried out using Merck alumina/silica gel 60-F254 (Merck 5554). Column chromatography was performed to purify the reaction products utilizing Merck Kieselgel 60 H silica gel (70 – 230 mesh).

2.2 Instrumentations

2.2.1 Fourier Transform Infrared Spectroscopy

FT-IR analyses were carried out to investigate detailed information about the chemical composition, polymeric structure, and functional groups in a non-destructive manner. The spectra were collected using a Perkin-Elmer 65 FT-IR spectrometer in transmission mode. The measurements were taken using both KBr pellets and ATR mode, with a scan rate of 4 cm^{-1} over a range of 4000 to 400 cm^{-1}. All analyses were carried out under ambient conditions.

2.2.2 Powder X-ray Diffraction

PXRD (Powder X-ray Diffraction) was used to demonstrate information on the crystalline structure and phase identification. The diffractograms were obtained using a Philips X'Pert Pro instrument and Bruker D8 Advance, with a Cu-Kα radiation source (k = 0.154 nm) operating at 45 kV and 40 mA. The patterns were obtained with a step size of 0.02 and a range of 2° to 60° 2ϴ.

2.2.3 Thermogravimetric Analysis

TGA (Thermogravimetric Analysis) was used for polymer characterization to analyze thermal stability and decomposition temperature insights. The Perkin Elmer Diomand TG/DTA was used to carry out this analysis. The samples were placed on a platinum pan and heated to 800 °C at a rate of 10 °C per minute under a nitrogen flow.

2.2.4 X-ray Photoelectron Spectroscopy

XPS (X-ray Photoelectron Spectroscopy) was performed to investigate surface chemical composition. ThermoFisher K-alpha spectrometer was used to perform this analysis. The samples were covered and pressed onto copper tape before analysis. The binding energy was calibrated by setting the adventitious carbon C 1s peak to 284.6 eV.

2.2.5 Energy Dispersive X-ray Spectroscopy and Scanning Electron Microscope

SEM and EDX were used to obtain high-resolution images of the polymer's surface morphology and to get elemental composition mapping. ZEISS EVO10 analyzer was used to analyze this characterization. SEM analysis was performed at 1.0-2.0 kV, while EDX analysis was conducted at 10-20 kV.

2.2.6 Nuclear Magnetic Resonance Spectroscopy

Nuclear Magnetic Resonance (NMR) Spectroscopy was used to obtain information about molecular structure, composition, and functional groups for synthesized monomers. The Varian Nuclear Magnetic Resonance Spectrometer (400 MHz) was used to record liquid phase ^{1}H NMR and ^{13}C NMR spectra. Deuterated solvents were used, and the measurements were taken at room temperature. Chemical shifts and coupling constants were given in ppm and Hz, respectively.

2.2.7 Gas Adsorption Measurements

Gas adsorption measurements were performed to demonstrate details about the surface area of the polymers, pore size distribution, and porosity of polymers, which are critical for understanding their adsorption properties. Micromeritics 3Flex analyzer was utilized for the gad adsorption analysis at 77 K. The samples were prepared for sorption data collection by degassing them for 12 hours at 120 °C under a dynamic vacuum. Brunauer-Emmett-Teller (BET) method was used to calculate the material's surface area. The valid relative pressure range for BET calculation was determined using Rouquerol plots.

2.2.8 Confocal Raman Spectrometer

Raman spectroscopy was performed via Renishaw via Qontor analyzer. Characterization of the solid material was measured using a 532 nm laser in x50 optical magnification. Measurements were taken over a wavenumber range of 3250 to 250 cm^{-1}.

2.3 Electrochemical Measurements and Sample Preparation

2.3.1 Preparation of Cathode Electrode

Preparation of the cathode, Quinone-Based Redox-Active Polymer (QRP-1 and QRP-2) was mixed with additives in specific proportions to enhance the electrode's conductivity. To achieve this, QRPs were mixed with polytetrafluoroethylene (PTFE, binder) and super P carbon black (a conductive reagent) in ethanol to create a uniform slurry. The weight ratio was 50% QRPs, 40% carbon black, and 10% PTFE.

2.3.2 Setting Up the Electrochemical Cell

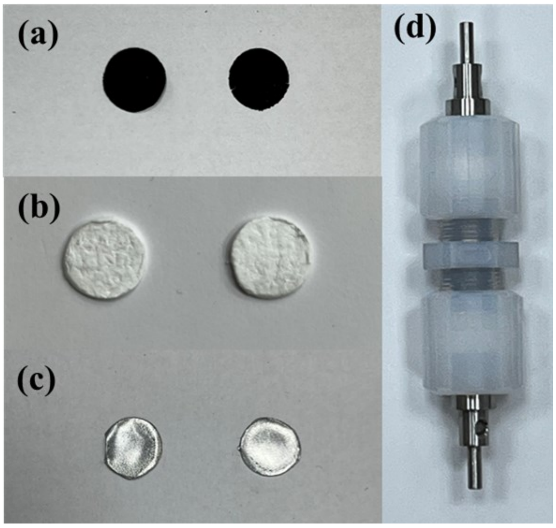

Figure 2.1. Materials used when assembling electrochemical cells: (a) QRPs (cathode), (b) Whatman filter paper (separator), (c) Zinc foil (anode), (d) Swagelok-type cell.

The electrochemical performance of the QRP-1 and QRP-2 cathode were tested using Swagelok-type cells with a two-electrode setup. Zinc foil anode (8 mm diameter), Whatman Glass Microfiber filter (separator), 1.0 M $ZnSO_4$ electrolyte, and QRP cathode electrodes were used to assemble the cells at room temperature. During the sealing of the cell, precautions were taken to prevent the tearing of the polymer-based cathode material.

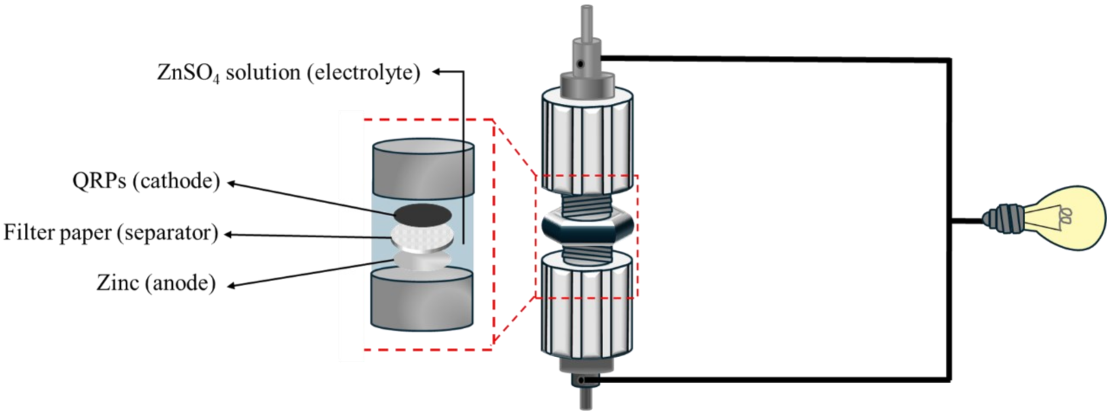

Figure 2.2. Schematic representation of materials inside a Swagelok-type cell.

2.3.3 Sample Characterizations and Instrumentation

The battery-cycler instrument, LANDT-CT3002A, was used to perform galvanostatic charge/discharge measurements within a potential range of 0.1 to 1.6 V. The cells were tested with cyclic voltammetry (CV) using a Gamry Instruments Interface 1010E potentiostat/galvanostat device. The CV profiles were collected within a potential window ranging from 0.1 to 1.6 V. The cells were stopped at 0.1 V and 1.6 V to examine the electrode in its discharged and charged states, respectively. The discarded electrodes were washed and then dried under vacuum. FT-IR, XPS, XRD, and EDX experiments were conducted to examine structural changes during charge and discharge measurements.

2.4 Monomer & Polymer Synthesis

2.4.1 Synthesis of QRP-2 Monomer

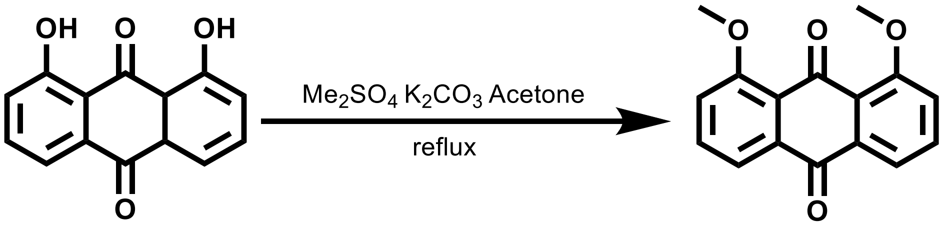

1,8-dihydroxy-9,10-anthraquinone

1,8-dimethoxy-9,10-anthraquinone

Figure 2.3. Synthesis route of 1,8-Dimethoxy-9,10-anthraquinone (procedure derived from Fritz and his colleagues).[72]

A 500 mL flask was charged with K_2CO_3 (16.1 g, 116 mmol) and acetone (300 mL) and stirred for 10 minutes. After that, 1,8-dihydroxy-9,10-anthraquinone (10.3 g, 43 mmol) was added to the solution and refluxed for 1 hour. During reflux, an acetone solution (40 mL) containing dimethyl sulfate (10.17 mL, 107 mmol) was gradually added to the reaction mixture over 40 minutes. The reaction was allowed to proceed at reflux for two days. After 48 hours, the reaction was stopped and cooled based on the TLC result. Subsequently, the reaction mixture was filtered, and the remaining residue was washed with DCM. The organic phases were filtered through a silica pad. The solvents were evaporated under reduced pressure, and the resulting residues were stirred in 2N NaOH for 30 minutes to remove dimethyl sulfate. The aqueous layers were extracted with DCM, and the solvents were evaporated. Yellowish product was obtained (89% yield, 10.26 g).

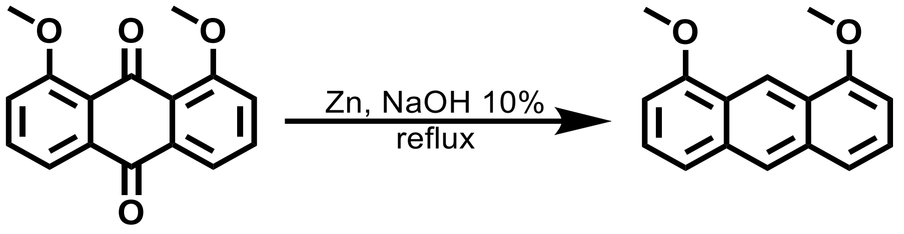

1,8-dimethoxy-9,10-anthraquinone 1,8-dimethoxyanthracene

Figure 2.4. Synthesis route of 1,8-Dimethoxyanthracene.[72]

A 500 mL flask was filled with 1,8-dimethoxy-9,10-anthraquinone (4.00 g, 14.88 mmol), zinc powder (5.84 g, 89.44 mmol), and 10% aqueous sodium hydroxide (100 mL). The reaction mixture was heated for one day. After 24 hours, the reaction mixture was filtered. Subsequently, the obtained grey-yellow precipitate was dissolved in DCM and filtered through a silica pad. After evaporating the solvent, the product was a yellow solid (80% yield, 2.8 g).

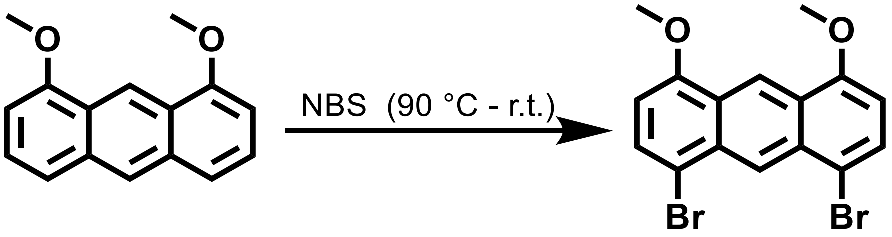

1,8-dimethoxyanthracene 1,8-dibromo-4,5-dimethoxyanthracene

Figure 2.5. Synthesis route of 1,8-Dibromo-4,5-dimethoxyanthracene.[72]

A 250 mL flask was charged with 1,8-dimethoxyanthracene (1.5 g, 6.3 mmol) in 75 mL DCM, then cooled to 0 °C. NBS (2.25 g, 12.9 mmol) was carefully added to the cooled reaction mixture. Then, the mixture was allowed to return to room temperature and was stirred for 4 hours. After stirring for 4 hours, the reaction mixture diluted with DCM was washed with 2N NaOH and water. Then, the organic phase was evaporated with the help of a vacuum. A green solid product was obtained (62% yield, 1.56 g).

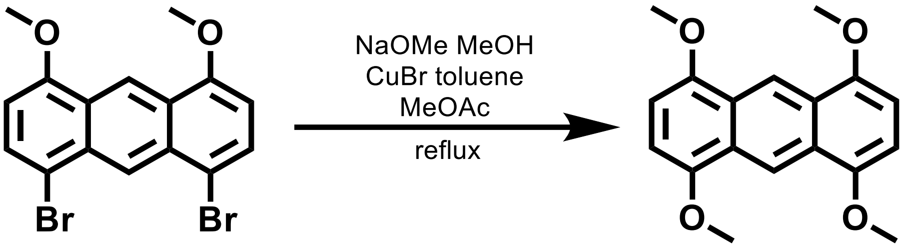

1,8-dibromo-4,5-dimethoxyanthracene 1,4,5,8-tetramethoxyanthracene

Figure 2.6. Synthesis route of 1,4,5,8-Tetramethoxyanthracene.[72]

A 250 mL flask was filled with 100 mL of methanol. Sodium (11.6 g, 0.5 mol) was added slowly to the methanol-containing flask for 1 hour. After adding sodium, the mixture was heated to 70 °C. Then, 1,8-dibromo-4,5-dimethoxyanthracene (2.0 g, 5.05 mmol), 50 mL dry toluene, MeOAc (4.76 g, 5.0 mL, 63.1 mmol), and copper (I) bromide (0.7 g, 5.05 mmol), was added to the reaction mixture. The reaction was allowed to reflux for 2 days. At the end of 48 hours, the reaction mixture was cooled to room temperature. Then, the solvents were evaporated and the residue was dissolved with DCM and washed with water containing 10% HCl. DCM was then evaporated, and the resulting solid was washed with hot chloroform to obtain a yellow solid product (40% yield, 0.6 g).

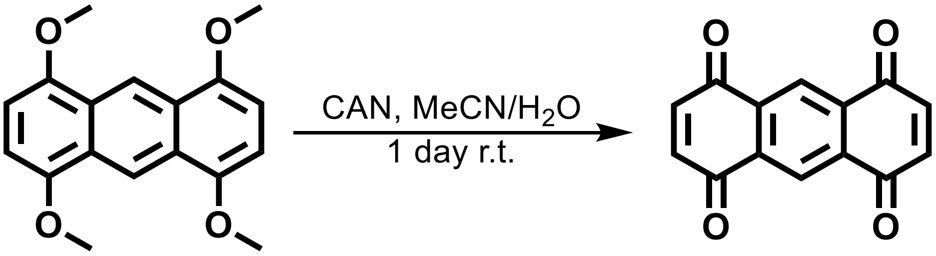

1,4,5,8-tetramethoxyanthracene 1,4,5,8-anthracenetetrone

Figure 2.7. Synthesis route of QRP-2 Monomer (1,4,5,8-Anthracenetetrone).[72]

A 50 mL round bottom flask was filled with cerium ammonium nitrate (8.7 g, 15.9 mmol) and 15 mL of water. After that, a solution of 1,4,5,8-tetramethoxy-anthracene (0.863 g, 2.9 mmol) in 22.5 mL MeCN was slowly added to the reaction mixture. Subsequently, the reaction mixture was stirred at room temperature for 24 hours. After one day, the reaction was complete, and the suspension was extracted with DCM. The organic phase was evaporated under pressure. The solid obtained from the experiment was purified by column chromatography. Red product was obtained after column chromatography (40% yield, 0.25 g). ^{1}H NMR (400 MHz, $CDCl_3$) δ (ppm) = δ 8.82 (s, 2H), 7.14 (s, 4H). ^{13}C NMR (100 MHz, $CDCl_3$): δ (ppm) = 183.3, 139.4, 135.12, 125.8.

2.4.2 Synthesis of Quinone-Based Redox-Active Polymer-1 (QRP-1)

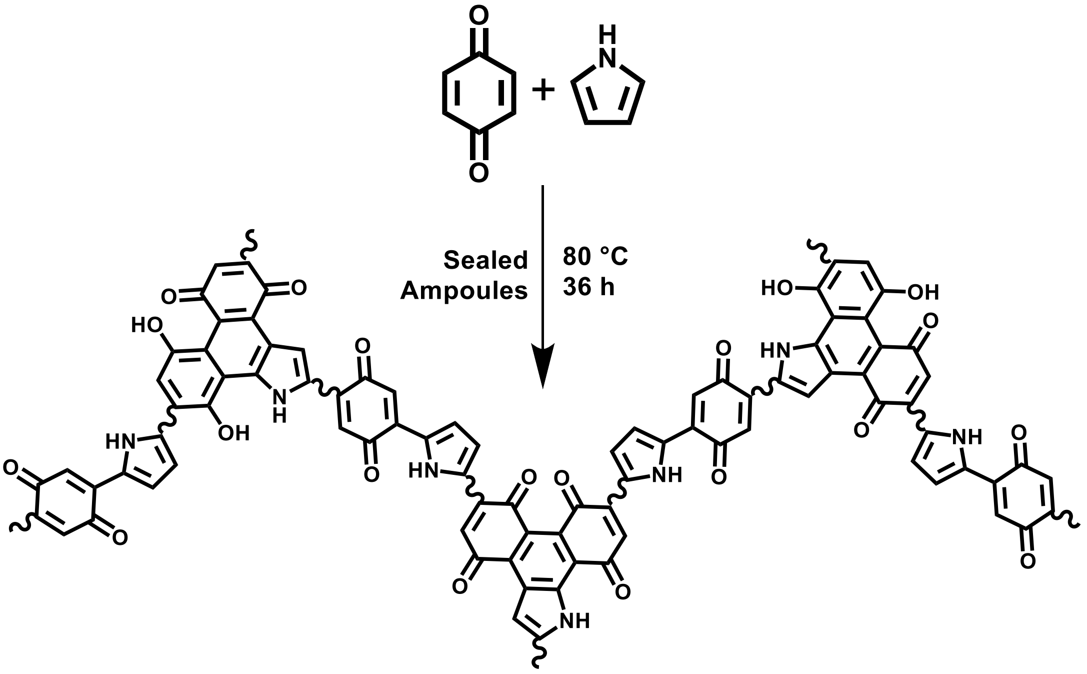

Figure 2.8. Synthesis route of QRP-1 (procedure derived from Chu and coworkers).[73]

Pyrrole (100 mg, 1.5 mmol) and benzoquinone (487 mg, 4.5 mmol) were added homogeneously into an ampoule to synthesize QRP-1. Then, the tip of the ampoule during vacuum was closed with the help of a blowtorch. The ampoule was kept in the oven at 80 °C for 36 hours. At the end of 36 hours, the solid formed as a result of the reaction was carefully removed from the ampoule. The extracted solid was washed with acetone to eliminate side products and dried at 90 °C (322.8 mg, 55%, black powder).

2.4.3 Synthesis of Quinone-Based Redox-Active Polymer-2 (QRP-2)

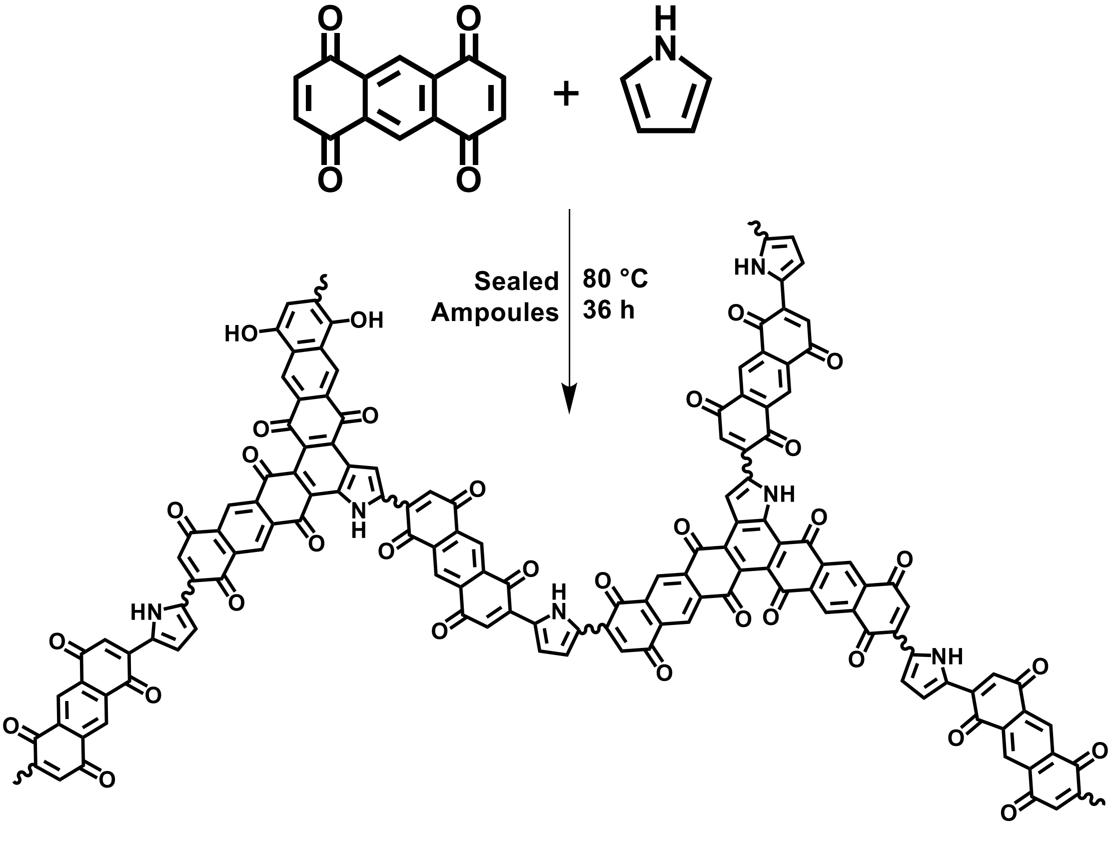

Figure 2.9. Synthesis route of QRP-2.

Pyrrole (100 mg, 1.5 mmol) and 1,4,5,8-anthracenetetrone (1071 mg, 4.5 mmol) were added homogeneously into an ampoule to synthesize QRP-2. Then, the tip of the ampoule during vacuum was closed with the help of a blowtorch. The ampoule was kept in the oven at 80 °C for 36 hours. At the end of 36 hours, the solid formed as a result of the reaction was carefully removed from the ampoule. The extracted solid was washed with acetone to eliminate side products and dried at 90 °C (316.8 mg, 27%, black powder).

CHAPTER 3

RESULTS AND DISCUSSION

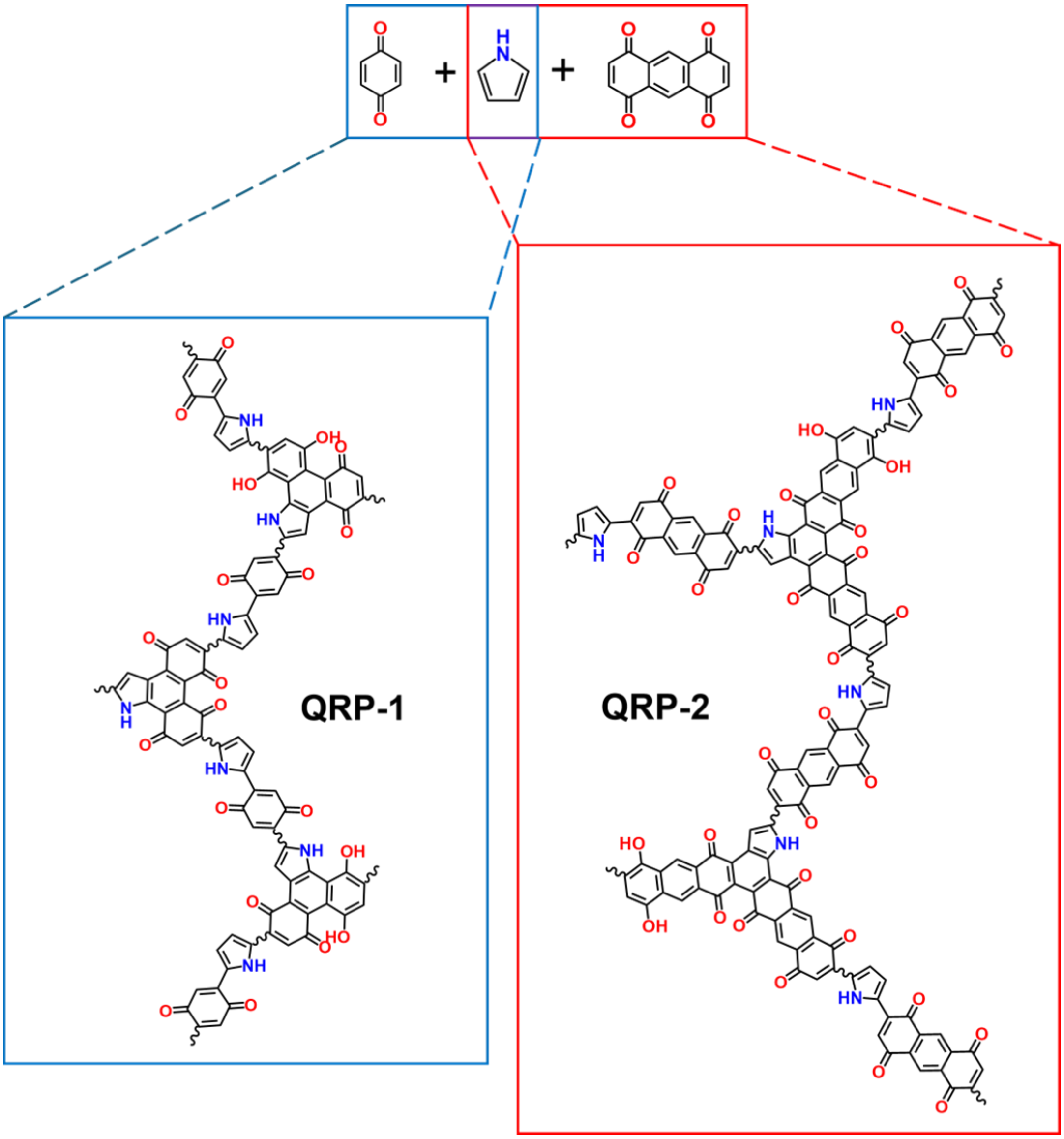

Figure 3.1. Synthetic route for QRP-1 and QRP-2.

As seen in Figure 3.1, the two synthesized polymers resulted from reactions between pyrrole and two different quinone derivatives. One starting material (pyrrole) was kept constant in this experiment, while two different quinone-based compounds were used as the other starting material (benzoquinone and 1,4,5,8-anthracenetetrone) to compare the applications of the two quinone-based polymers (QRP-1 and QRP-2) in the field of electrochemistry. The method used in this study is both cost-effective and environmentally friendly because it avoids the use of heavy metal catalysts or organic solvents. The ampoule sealing experiment is conducted because quinone and pyrrole compounds are known for their low sublimation and boiling temperature. Proper sealing of the ampoules was crucial to prevent exposure to air and moisture, as quinone/pyrrole groups are sensitive to oxidation and hydrolysis.

3.1 Characterization of QRP-1 and QRP-2

Characterizations, including Fourier-transform infrared (FT-IR) spectroscopy, X-ray photoelectron spectroscopy (XPS), Powder X-ray diffraction (PXRD), Thermogravimetric analysis (TGA), Raman spectrometer, Scanning electron microscope (SEM) and Energy dispersive X-ray spectroscopy (EDX), were used to confirm the formation of the desired polymers.

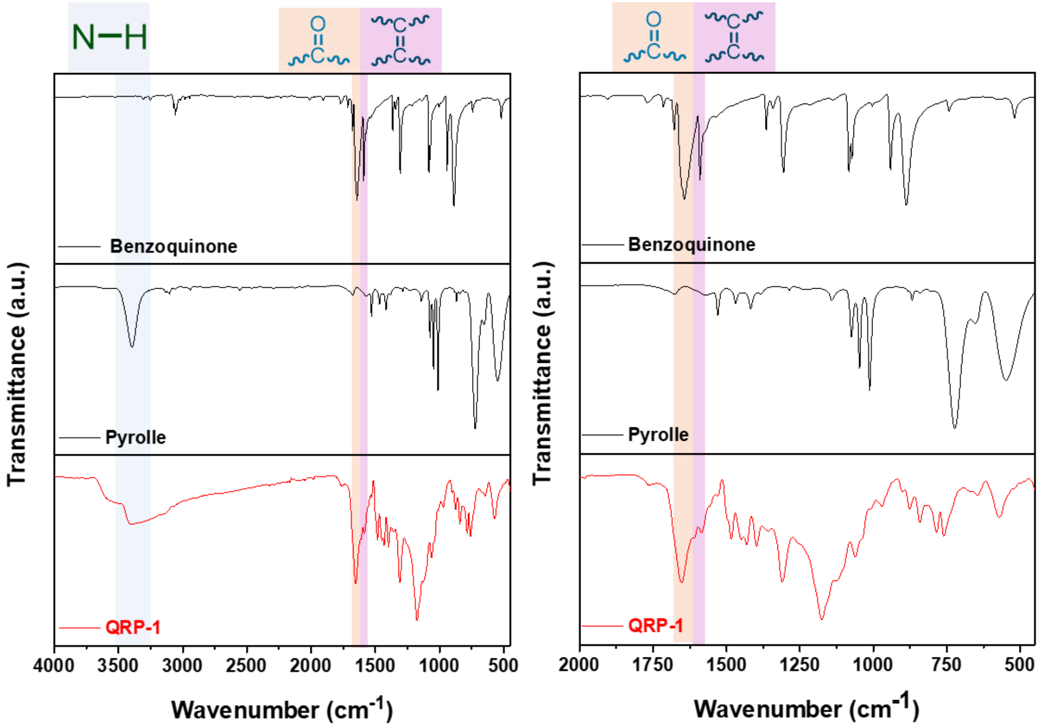

Figure 3.2. FT-IR spectra of benzoquinone, pyrolle, and QRP-1.

In the FT-IR spectra of QRP-1, an N-H stretching band appears at 3400 cm^{-1}. Similarly, the N-H stretching band in pyrrole's spectra is observed at 3400 cm^{-1}.

Furthermore, the C=O stretching observed near 1650 cm^{-1} and the C=C stretching around 1580 cm^{-1} are consistent with the proposed structure (Figure 3.2).

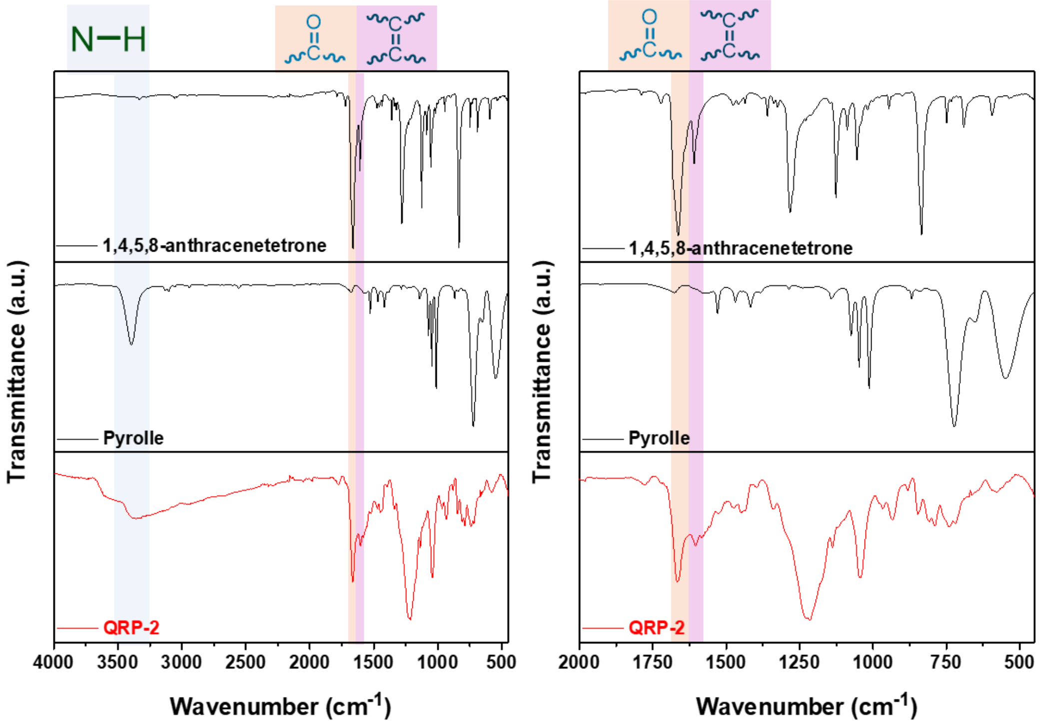

Figure 3.3. FT-IR spectra of 1,4,5,8-anthracenetetrone, pyrolle, and QRP-2.

In the FT-IR spectra of QRP-2, C=O, and C=C stretching bands appear at 1670 cm^{-1} and 1605 cm^{-1}, respectively. This result is supported by the spectra of 1,4,5,8-anthracenetetrone, which show C=O and C=C stretching bands at the same wavenumbers. Moreover, the C-N stretching observed near 3200 cm^{-1} matches the proposed structure (Figure 3.3).

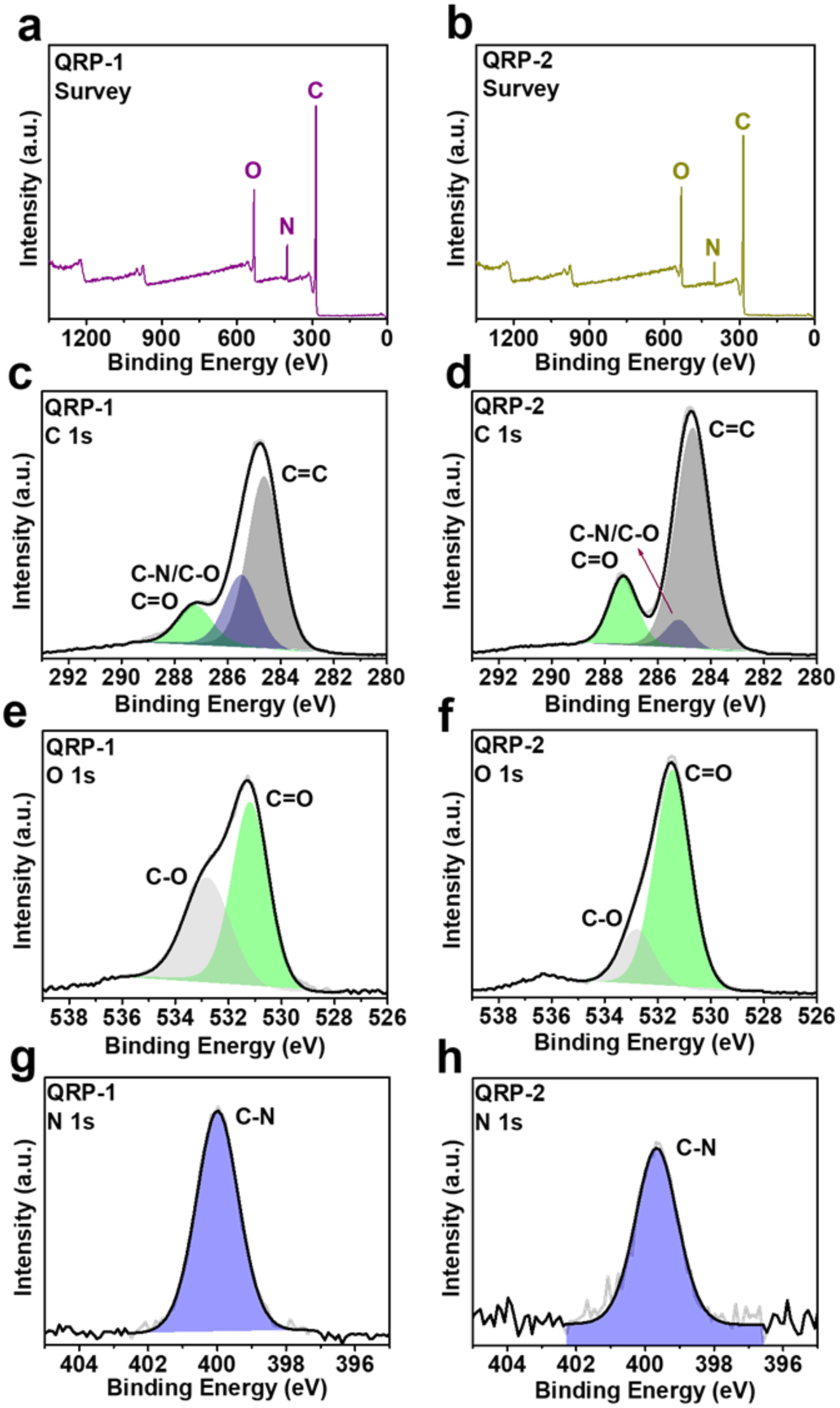

Figure 3.4. XPS analysis of QRP-1 and QRP-2 (a) survey spectrum of QRP-1, (b) survey spectrum of QRP-2, (c) C 1s high.resolution spectra of QRP-1, (d) C 1s high.resolution spectra of QRP-2, (e) O 1s high.resolution spectra of QRP-1, (f) O 1s high.resolution spectra of QRP-2, (g) N 1s high.resolution spectra of QRP-1, (h) N 1s high.resolution spectra of QRP-2.

The XPS technique is utilized to examine the structure of the polymers and types of chemical bonding. The survey scan analysis is used as an initial step to identify the elements present in the polymeric structure (Figure 3.4 (a) and (b)). The efficient purification of both proposed structures, QRP-1 and QRP-2, is demonstrated by detecting the 1s signals of oxygen, carbon, and nitrogen atoms. High-resolution XPS spectra were examined to determine the chemical states of carbon, oxygen, and nitrogen atoms. The deconvolution of the high-resolution C 1s spectra of QRP-1 and QRP-2 revealed three peaks at 284.6, 285.5, and 287.3 eV (Figure 3.4 (c) and (d)). The peak at 284.6 eV is linked to carbon atoms in aromatic rings (C=C), while the peak at 285.5 eV corresponds to C-N (carbon-nitrogen) and C-O (carbon-oxygen) bonds. The peak at 287.3 eV is associated with carbon atoms in the carbonyl group (C=O). The high-resolution O1s spectra of QRP-1 and QRP-2 were deconvoluted into two peaks at 531.2 and 532.8 eV. The peak at 531.2 eV corresponds to oxygen atoms in the carbonyl group (C=O), while the peak at 532.8 eV is associated with oxygen atoms in C-O bonds (Fig. 3.4 (e) and (f)). The peak at about 399.8 eV in the high-resolution N 1s spectra of QRP-1 and QRP-2 corresponds to nitrogen atoms in C-N bonds (Fig. 3.4 (g) and (h)).

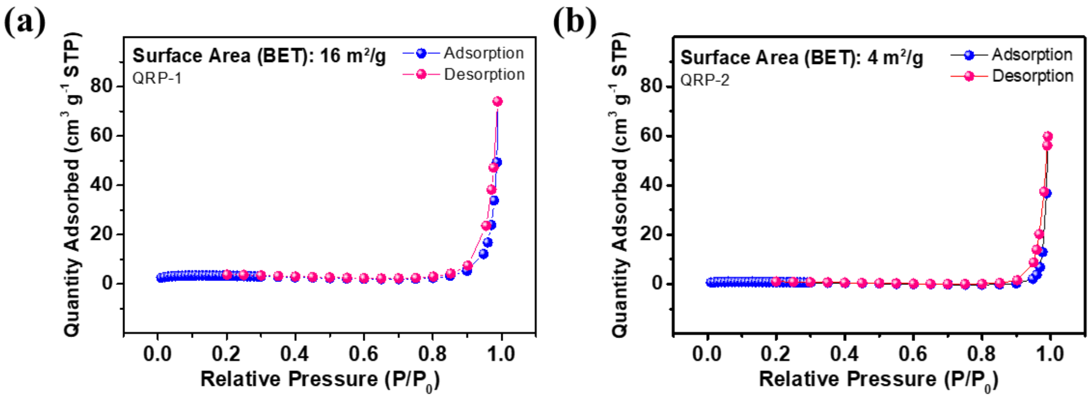

Figure 3.5. Adsorption/desorption isotherm of QRP-1 (a), and QRP-2 (b) collected using N_2 at 77 K.

The porosity of the polymer was examined by conducting N_2 sorption experiments at 77 K, as shown in Figure 3.5. The QRP-1 and QRP-2 showed type III isotherms characterized by a rapid increase in adsorption at high partial pressure.

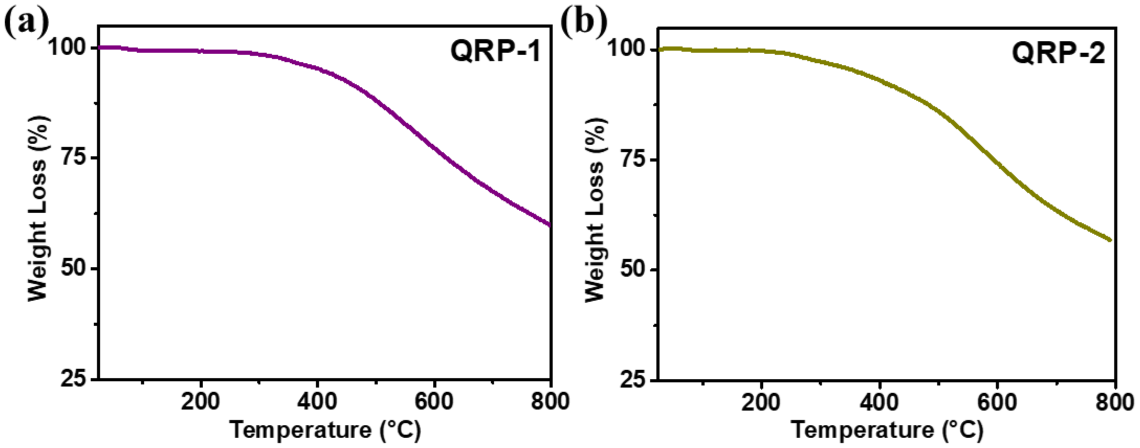

Figure 3.6. TGA Analysis in a Nitrogen Atmosphere (a) QRP-1, (b) QRP-2.

Thermogravimetric analysis (Figure 3.6) was utilized to investigate the thermal stability of the proposed polymers. Before the tests, samples undergo degassing to eliminate any organic solvents and moisture that may have been trapped therein. The two graphs clearly show that the polymer remains stable and does not lose any mass up to 300°C. Between 300°C and 500°C, there are only minor mass losses of about 12%. However, after 500°C, there is a significant mass loss, with only 60% of the mass remaining at 800°C. These results indicate that both QRP-1 and QRP-2 have excellent thermal stability up to 300°C.

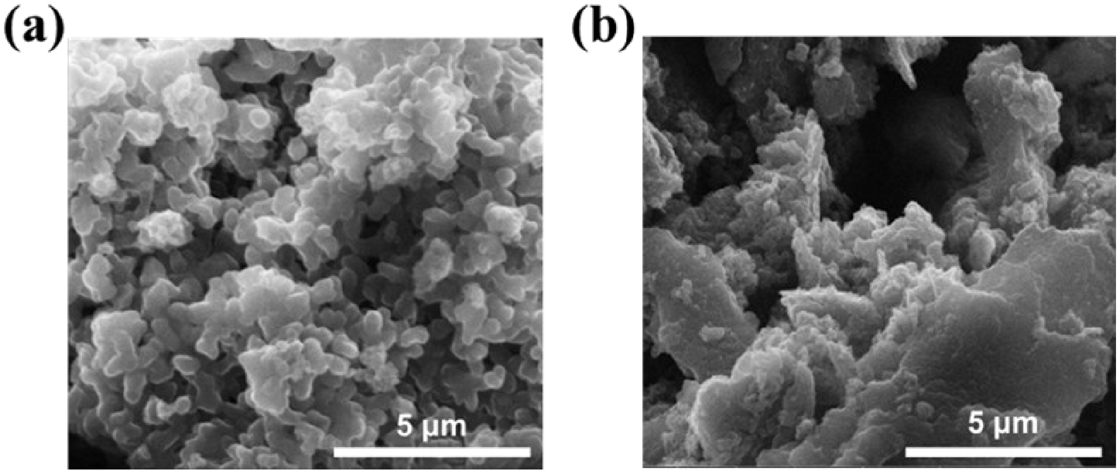

Figure 3.7. SEM images of (a) QRP-1 and (b) QRP-2.

The particle shapes of QRP-1 and QRP-2 were studied using scanning electron microscopy (SEM) (Figure 3.7). The SEM images reveal spherical particles with diameters of about 250 nm.

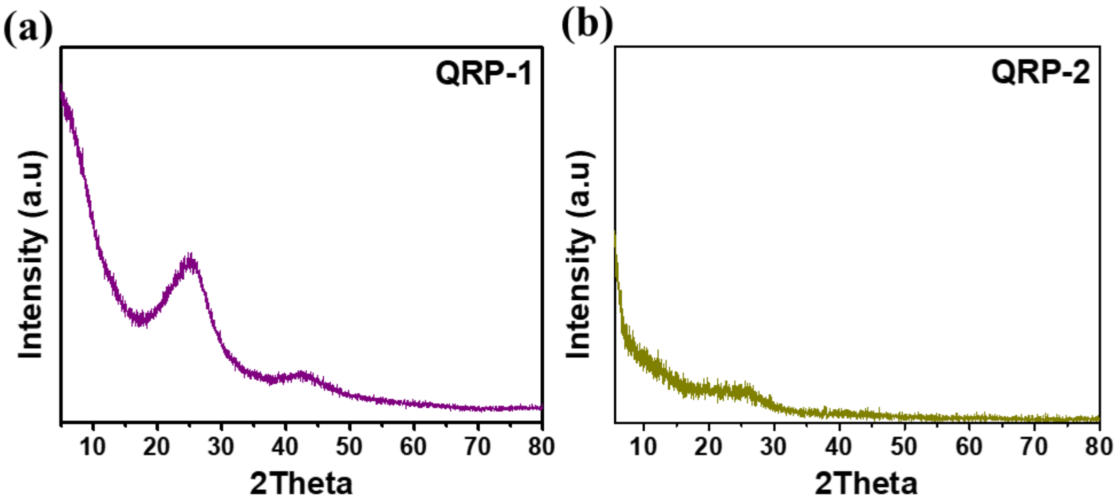

Figure 3.8. PXRD pattern of (a) QRP-1 and (b) QRP-2.

Powder X-ray diffraction analysis (PXRD) was conducted to check for crystallinity in the polymeric networks (Figure 3.8). Both polymeric structures are suggested to be amorphous due to the absence of sharp peaks in the diffractogram.

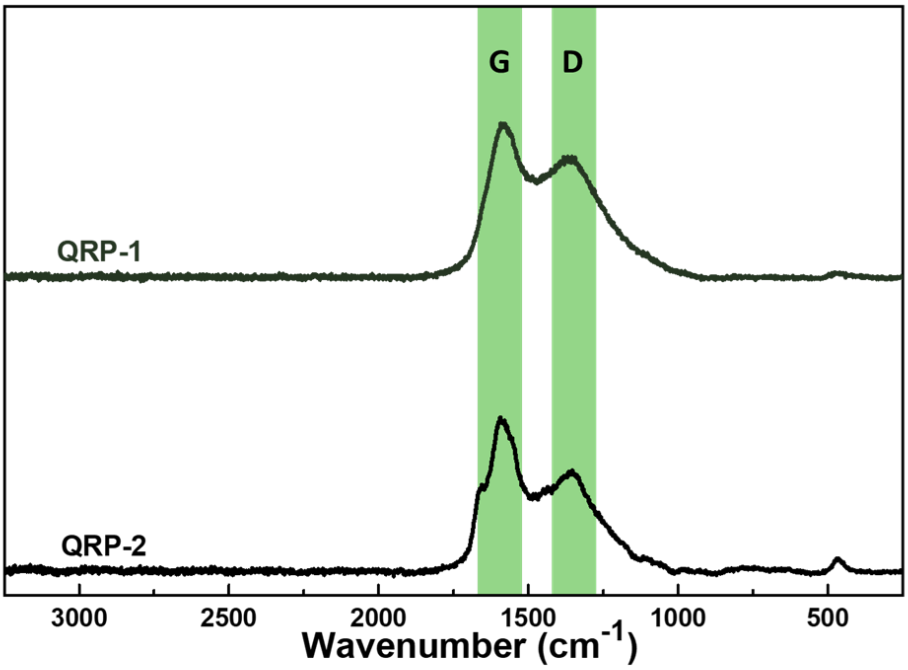

Figure 3.9. Raman spectra of QRP-1 and QRP-2.

Raman measurements of QRP-1 and QRP-2 are shown in Figure 3.9. The Raman spectra show G and D bands at about 1580 and 1380 cm^{-1}, confirming that both polymers have similar conjugated structures.

3.2 Electrochemical Performance of QRP-1 and QRP-2.

The initial evaluation of the reversibility of ion insertion and extraction in the QRPs was conducted using cyclic voltammetry (CV). At various scan rates, the CV measurements were recorded within the potential window of 0.1 to 1.6 V. Oxidation peaks at 0.81, 1.02, and 1.33 V. Two reduction peaks at 0.86, and 0.64 V are shown in the voltammograms, confirming the reversibility of the QRP-1 electrode and corresponding to the redox reaction at the cathode (Figure 3.10 (a)). In QRP-2, three oxidation peaks were observed at 0.66, 0.92 and 1.13 V, while three reduction peaks were detected at 0.94, 0.72, and 0.52 V (Figure 3.10(b)).

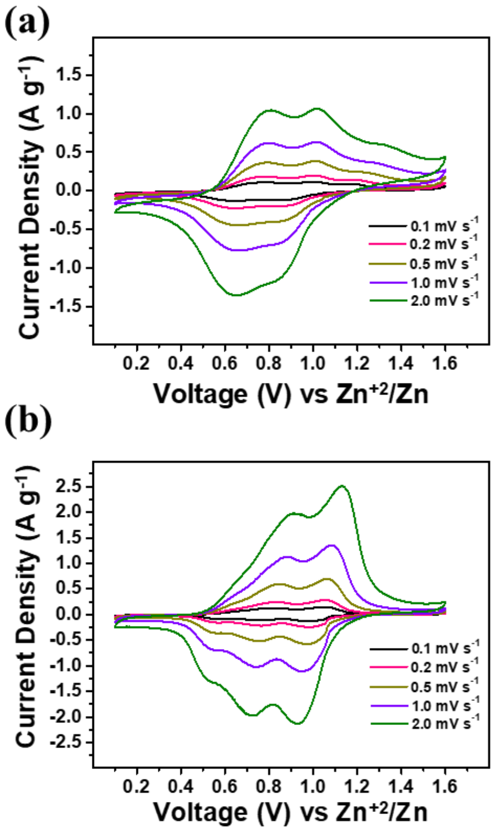

Figure 3.10. Cyclic voltammetry (CV) curves for (a) QRP-1 and (b) QRP-2.

When the scan rate increases, it is worth noting that the anodic and cathodic peak currents also increase, while the peak positions show minimal change. This indicates the rapid kinetics and reversibility of ion insertion and extraction.

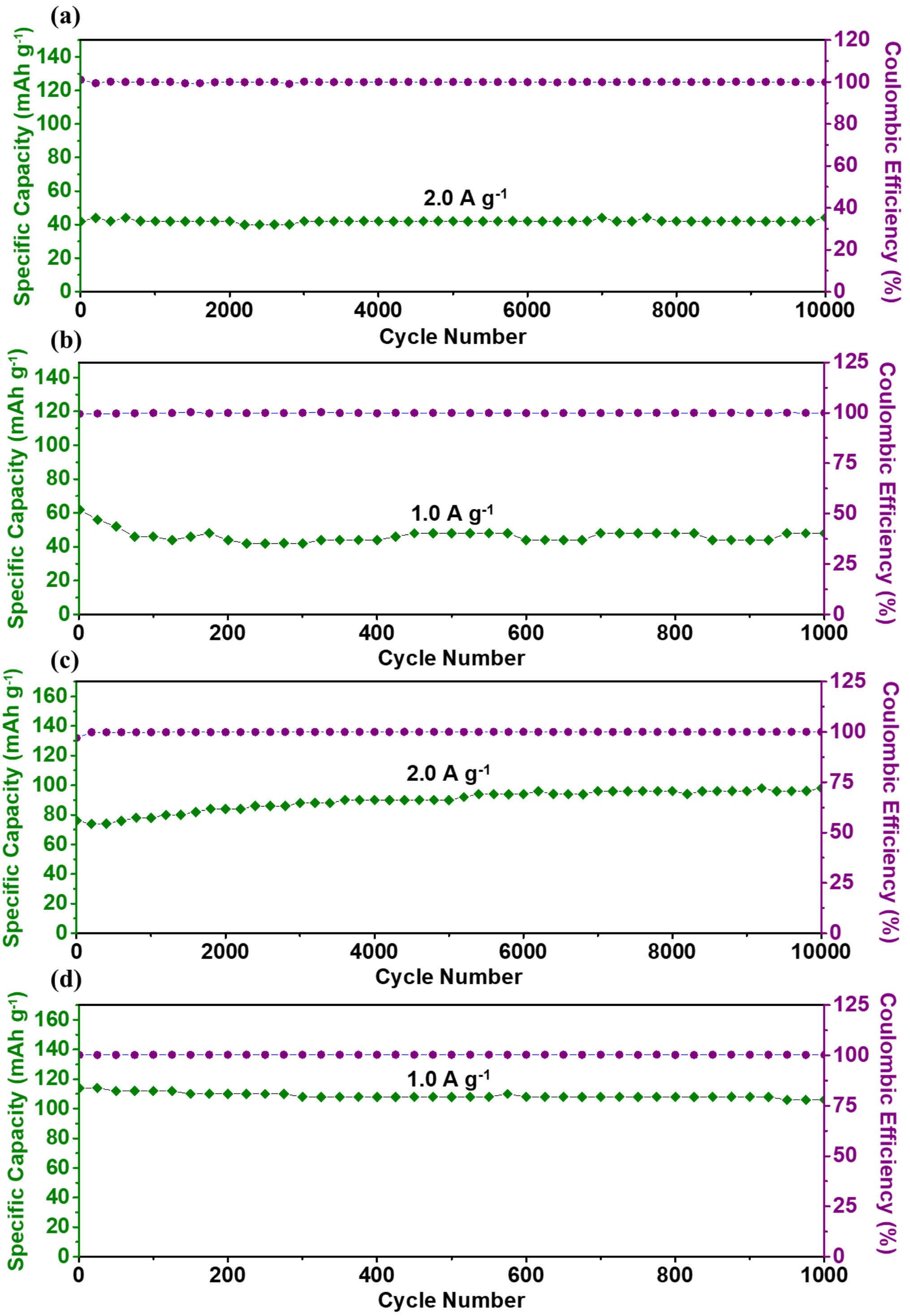

Figure 3.11. Cycle life of QRP-1 cathode at (a) 2.0 A g^{-1} and (b) 1.0 A g^{-1}, and cycle life of QRP-2 cathode at (c) 2.0 A g^{-1} and (d) 1.0 A g^{-1}.

The long-term cycling stability of the QRP-1 and QRP-2 electrodes was tested at different current densities. Both QRP-1 and QRP-2 demonstrated coulombic efficiency of 100%. The QRP-1 electrode was subjected to testing at a current density of 2.0 A g^{-1} for a duration of 10000 cycles (Figure 3.11(a)). The specific capacity, initially measured at 42 mAh g^{-1}, fluctuated between 38 and 44 mAh g^{-1} throughout 10000 cycles, ultimately stabilizing at 42 mAh g^{-1} at the end of the testing period. Then, the same electrode was tested at a current density of 1.0 A g^{-1} for 1000 cycles (Figure 3.11(b)). The specific capacity, initially measured at 62 mAh g^{-1}, settled at 48 mAh g^{-1} by the end of the testing period. The QRP-2 electrode, similar to QRP-1, was subjected to 10,000 cycles at a current density of 2.0 A g-1 (Figure 3.11(c)). The specific capacity, initially measured at 76 mAh g^{-1}, experienced a slight decrease to 74 mAh g^{-1} by the 400th cycle. However, after the 500th cycle, the activated electrode began to show an upward trend. By the end of the 10000 cycles, it achieved a notable result of 104 mAh g^{-1}. Subsequently, the same activated QRP-2 electrode was tested at a current density of 1.0 A g^{-1} for 1000 cycles (Figure 3.11(d)). The specific capacity, initially 114 mAh g^{-1}, slightly declined to 106 mAh g^{-1} by the end of the 1000 cycles. These results show that the QRP electrodes in ZIBs have long-term solid cycling stability and maintain their structure during prolonged charge and discharge cycles.

Galvanostatic charge-discharge (GCD) measurements were performed to examine the performance at different current densities, charge storage capacity, and long-term cycling stability of the QRP-1, and QRP-2 electrodes. Initially, the capacity of the QRP electrodes was assessed by applying different current densities. At a current density of 0.1 A g^{-1}, the cell with the QRP-1 cathode delivered discharge capacities of 180 mAh g^{-1} (Figure 3.12(a)). The cell with the activated QRP-2 cathode delivered discharge capacities of 134 mAh g^{-1} at a current density of 0.1 A g^{-1} (Figure 3.12(b)). These values demonstrate the excellent charge storage capacity of both QRPs in ZIBs.

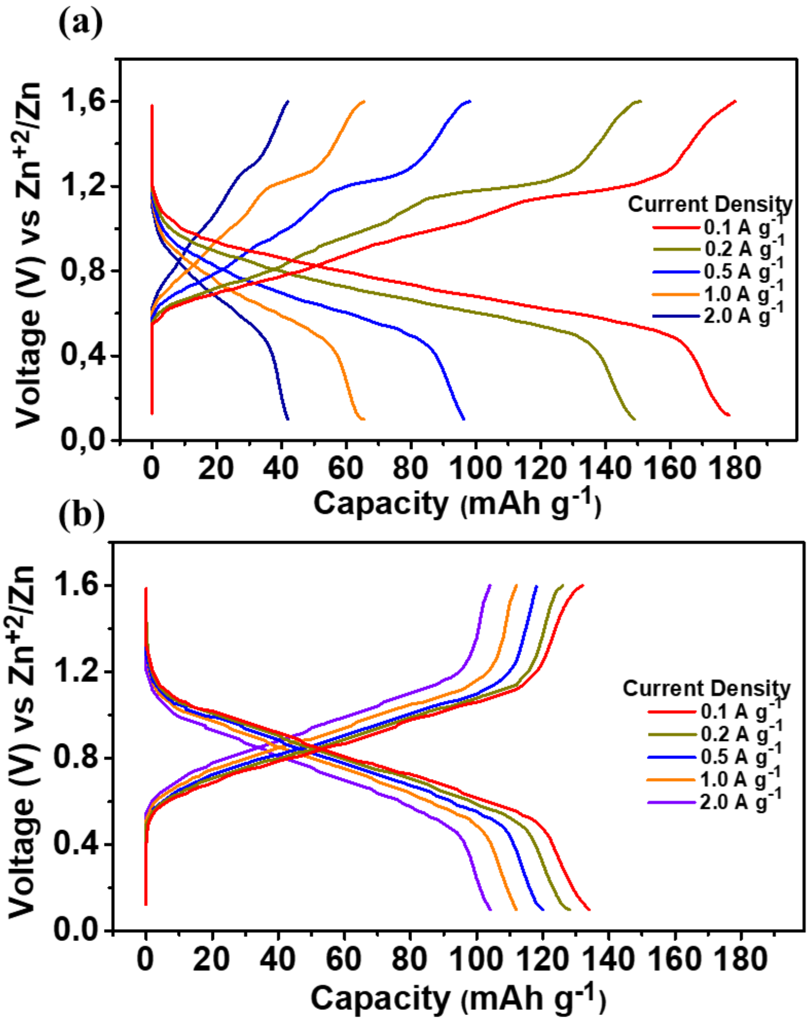

Figure 3.12. Galvanostatic charge and discharge measurements at different current densities (a) QRP-1, (b) QRP-2.

The rate capability of both QRP electrodes was tested at different current densities. For the QRP-1 electrode, discharge capacities were 180, 151, 98, 65, and 42 mAh g^{-1} as the current density increased to 0.1, 0.2, 0.5, 1.0, and 2.0 A g^{-1}, respectively (Figure 3.12(a)). Similarly, the QRP-2 electrode showed discharge capacities of 134, 128, 120, 112, and 104 mAh g^{-1} at the same current densities (Figure 3.12(b)). When the current density was reduced back to 0.1 A g^{-1} from 2.0 A g^{-1}, QRP-1 recovered 92% of its original capacity (165 mAh g^{-1}), while QRP-2 fully recovered its capacity. These values demonstrate the excellent high-rate performance of both QRP-1 and QRP-2 electrodes in ZIBs.

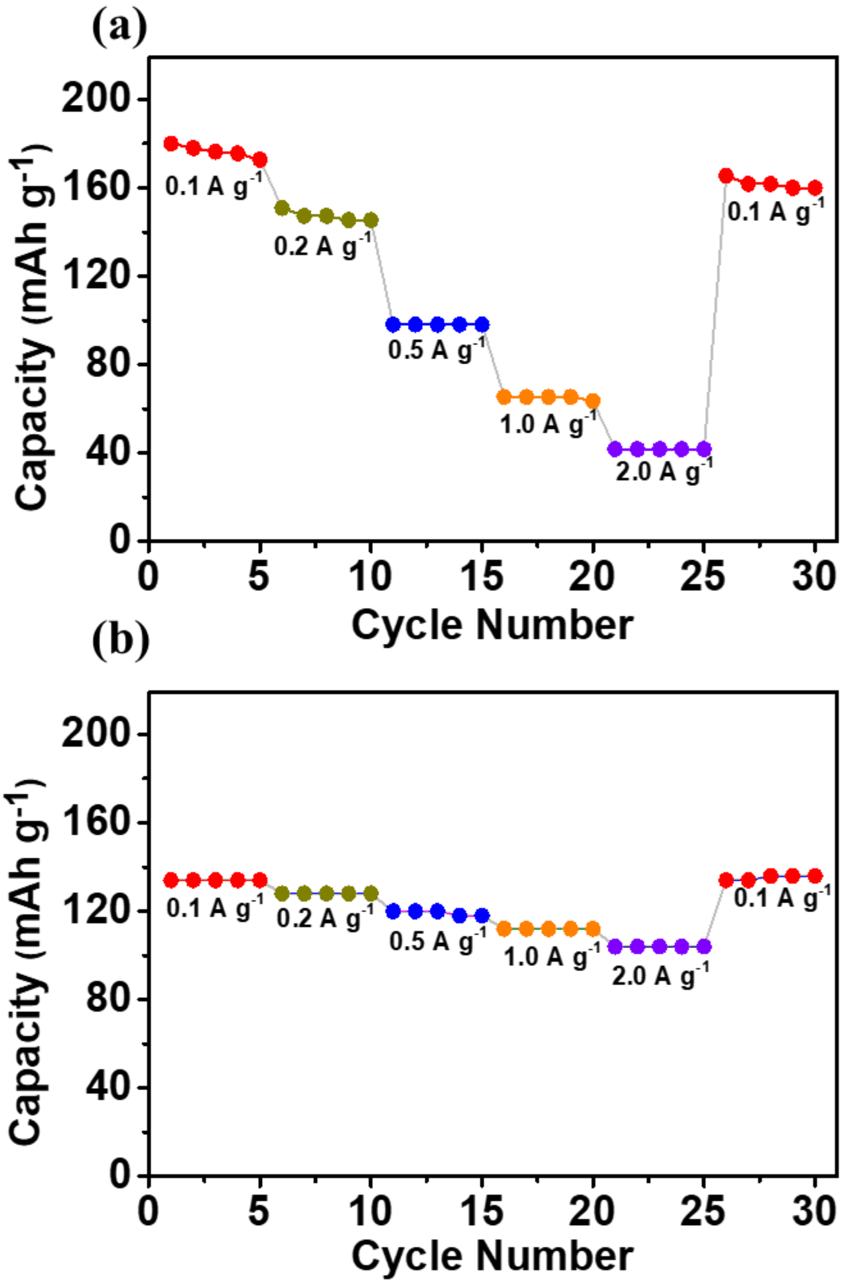

Figure 3.13. Rate performance of (a) QRP-1 and (b) QRP-2 cathode.

3.3 Electrochemical Kinetics of QRP-1 and QRP-2.

The electrochemical kinetics of the QRP-1 (Figure 3.14(a)) and QRP-2 (Figure 3.14(c)) cathode were revealed through CV measurements performed at various sweep rates. The power-law equation, $i = av^b$, enables the estimation of the *b*-value by examining how the peak current (i) in amperes (A) relates to the scan rate (v) in volts per second (V s^{-1}). The *b*-values are calculated between 0.5 and 1.0. A *b*-value near 0.5 signifies the charge storage behavior characteristic of a battery, where the process is controlled by diffusion. Also, this type of diffusion-controlled process is called the faradaic process. On the other hand, a *b*-value closer to 1.0 indicates that a non-faradaic process controls charge storage. This type of non-faradaic process is called capacitive-controlled. In the calculations made for QRP-1 and QRP-2, *b*-values are obtained by examining the linear slopes of log *i* and log *v*, and these results are used to examine the charge storage characteristic of the reactions taking place at the cathode. The *b*-values for QRP-1 were determined as follows: for the three oxidation peaks at 0.81, 1.02, and 1.33 V, the b-values were calculated to be 0.74, 0.72, and 0.55, respectively. For the reduction peaks at 0.86 and 0.64 V, the corresponding b-values were 0.74 and 0.77, respectively (Figure 3.14(b)). For QRP-2, the b-values were calculated as follows: 0.81, 0.92, and 0.96 for the oxidation peaks at 0.66, 0.93, and 1.13 V, respectively. For the three reduction peaks at 0.52, 0.72, and 0.94 V, the corresponding *b*-values were 0.90, 0.94, and 0.92, respectively (Figure 3.14(d)).

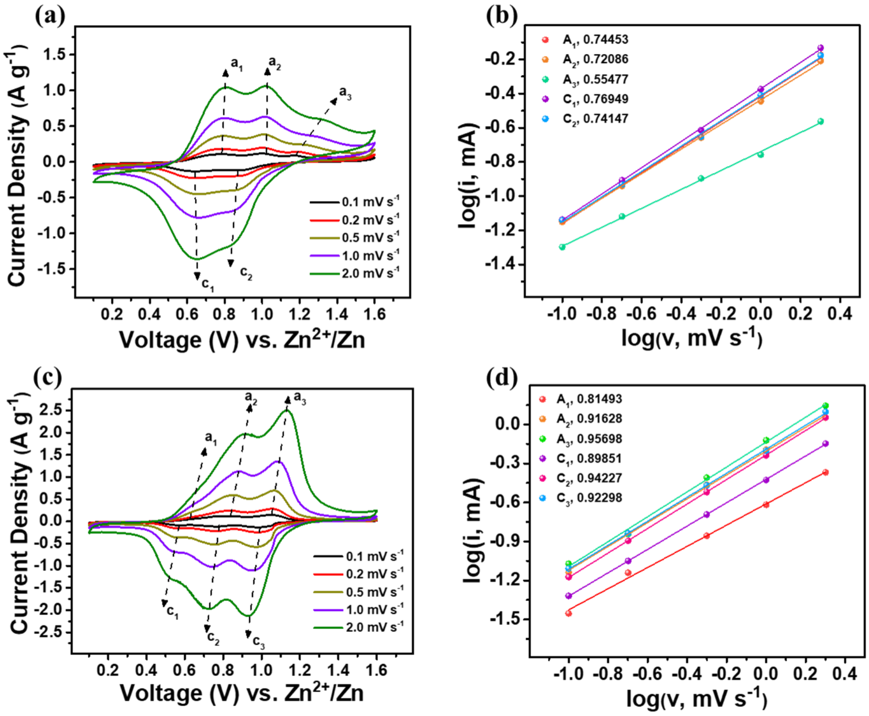

Figure 3.14. Kinetics of electrochemical measurements for QRPs: CV curves at different scan rates for QRP-1(a) and QRP-2(c), *b*-values for cathodic/anodic peaks based on the power law equation QRP-1(b) and QRP-2(d).

If the *b*-value is greater than 0.8, this can be interpreted as capacitive process charge storage being more dominant than the diffusion-controlled.[74] Observed *b*-values support the idea that QRP-2 exhibits a capacitive charge storage mechanism. In QRP-1, although the results do not show that a capacitive-controlled process is progressing as high as in QRP-2, they support that QRP-1 shows capacitive-controlled and diffusive-controlled processes together. This suggests that faradaic redox reactions play an important role in the charge storage of QRP-1. The equation [$i(\mathrm{V}) = \mathrm{k}_1 \nu + \mathrm{k}_2 \nu^{1/2}$], established by Dunn and colleagues, is used for the precise distinction between the faradaic process and the non-faradaic process at specific potentials. The equation describes the relationship between the total current (i) and the potential (V). It states that the total current is a result of two separate mechanisms: capacitive effects ($\mathrm{k}_1 \nu$) and diffusion-controlled insertion ($\mathrm{k}_2 \nu^{1/2}$).

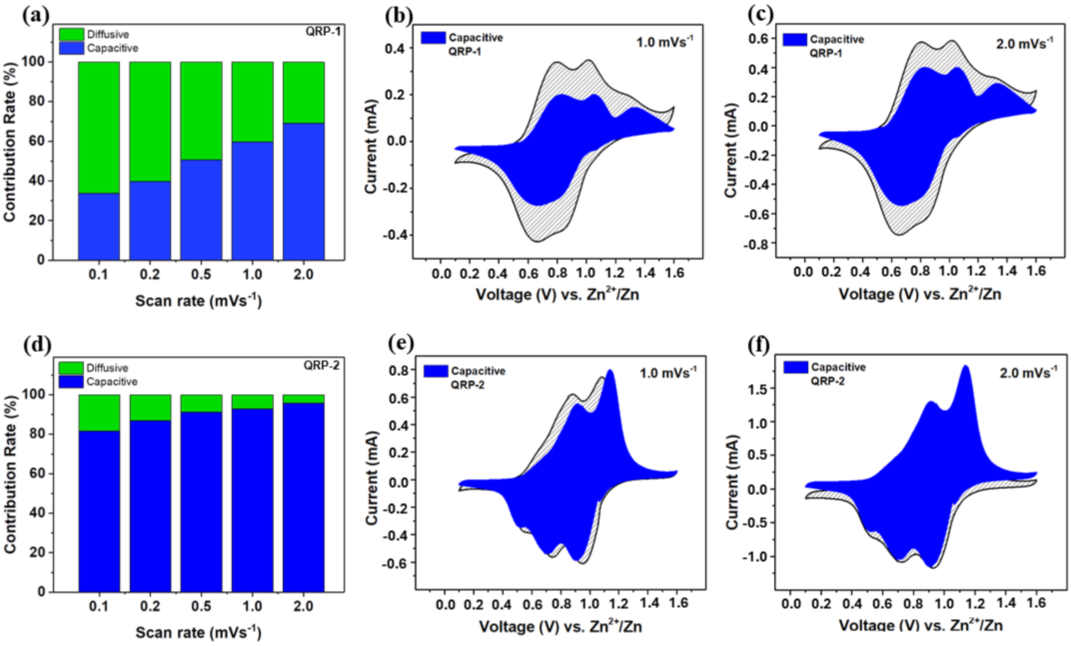

Figure 3.15. Capacitive and diffusive current contributions to charge storage at scan rates from 0.1 to 2.0 mV s^{-1} (a)QRP-1 and (d) QRP-2. Contributions of capacitive currents to the charge storage of QRP-1 at scan rates ranging from 1.0 mV s^{-1} (b) to 2.0 mV s^{-1} (c). Contributions of capacitive currents to the charge storage of QRP-2 at scan rates ranging from 1.0 mV s^{-1} (e) to 2.0 mV s^{-1} (f)

As shown in Figure 3.15, for QRP-1, the capacitive contribution values at scan rates of 0.1, 0.2, 0.5, 1.0, and 2.0 mV s^{-1} are 34%, 40%, 51%, 60%, and 69%, respectively. These findings demonstrate an increasing capacitive contribution with higher scan rates. Similarly, for QRP-2, the corresponding capacitive contribution values at the same scan rates are 82%, 87%, 91%, 93%, and 96%.

3.4 Charge Storage Mechanisms of QRP-1 and QRP-2

Ex-situ characterization methods were used for QRP-1 and QRP-2 electrodes for their charged and discharged states to investigate the charge storage mechanism. To accomplish this, the battery tests stopped when the voltage reached 1.6 V (charged state) and 0.1 V (discharged state), and the electrodes were removed from the cell, washed with water, and dried.

3.4.1 Formation of Zinc Hydroxy Sulfate Salt

In previous works on zinc ion batteries, researchers have shown that the electrochemical reactions occurring at the cathode not only involve zinc ions but also require protons as secondary charge carriers in electrolytes with mildly acidic pH.[60,75] During the discharge process, the carbonyl units accommodate protons, which results in to increase in the pH of the electrolyte. This increase in pH supports the formation of zinc hydroxy sulfate [$Zn_4SO_4(OH)_6 \cdot nH_2O$] as a side product on the surface of the cathode. Previous studies support that the formation of [$Zn_4SO_4(OH)_6 \cdot nH_2O$] salt on the cathodes in the discharge state was observed as a result of ex-situ analyses, while the findings of the [$Zn_4SO_4(OH)_6 \cdot nH_2O$] salt on the electrodes in the charged state decreased or completely disappeared. This shows that the formation of the [$Zn_4SO_4(OH)_6 \cdot nH_2O$] salt is a reversible process.[75]

3.4.2 Ex-Situ Characterizations of QRP-1 and QRP-2

The changes in structure that occur during the charge storage of the QRP-1 and QRP-2 cathodes are analyzed using ex-situ methods. During the initial phase, the identification of the functional groups responsible for the binding of ions is achieved by studying the discharged electrode using Fourier Transform Infrared analysis.

When the electrode is discharged at 0.1 V, a major decrease in the intensity of the carbonyl stretching band at approximately 1650 cm^{-1} is detected for both polymers. This observation indicates that the quinone groups are involved in redox reactions (Figure 3.16). This decrease in the intensity of the carbonyl stretching band is reversed and the corresponding peak to the carbonyl stretching band reappears when the electrode is charged state at 1.6 V. This reappearance provides evidence for the reversibility of ion accommodation.

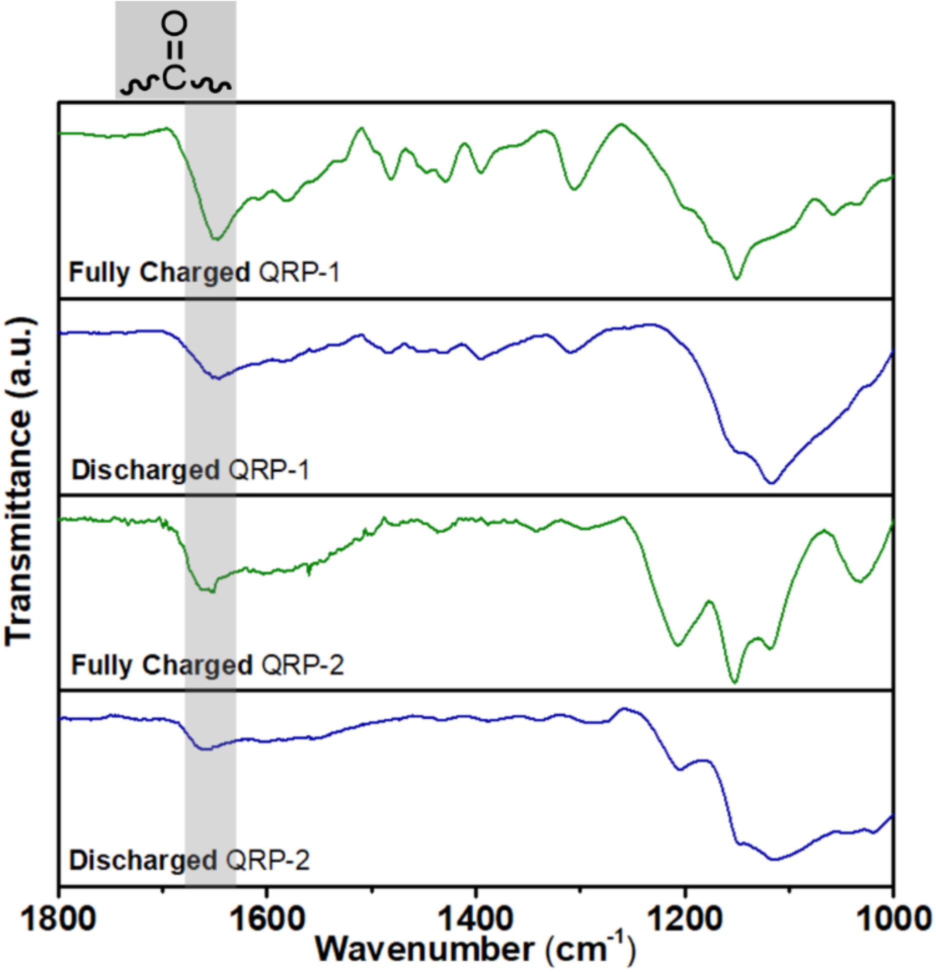

Figure 3.16. FT-IR spectra of QRP-1 and QRP-2 at charged and discharged states.

To examine the co-insertion behavior of Zn^{2+}/H^+ and the elemental composition of the cathode, Energy dispersive X-ray mapping was performed on the exact SEM region. Oxygen, nitrogen, carbon, sulfur, and zinc were obtained homogeneously at the discharged state for both polymers (Figure 3.17). Sulfur and zinc signal on the EDX, nearly vanish for charging states at 1.6 V for both QRP-1 and QRP-2, indicating reversible co-insertion behavior of Zn^{2+}/H^+ and the dissolution of the [Zn4SO4(OH)6·nH2O] salt.

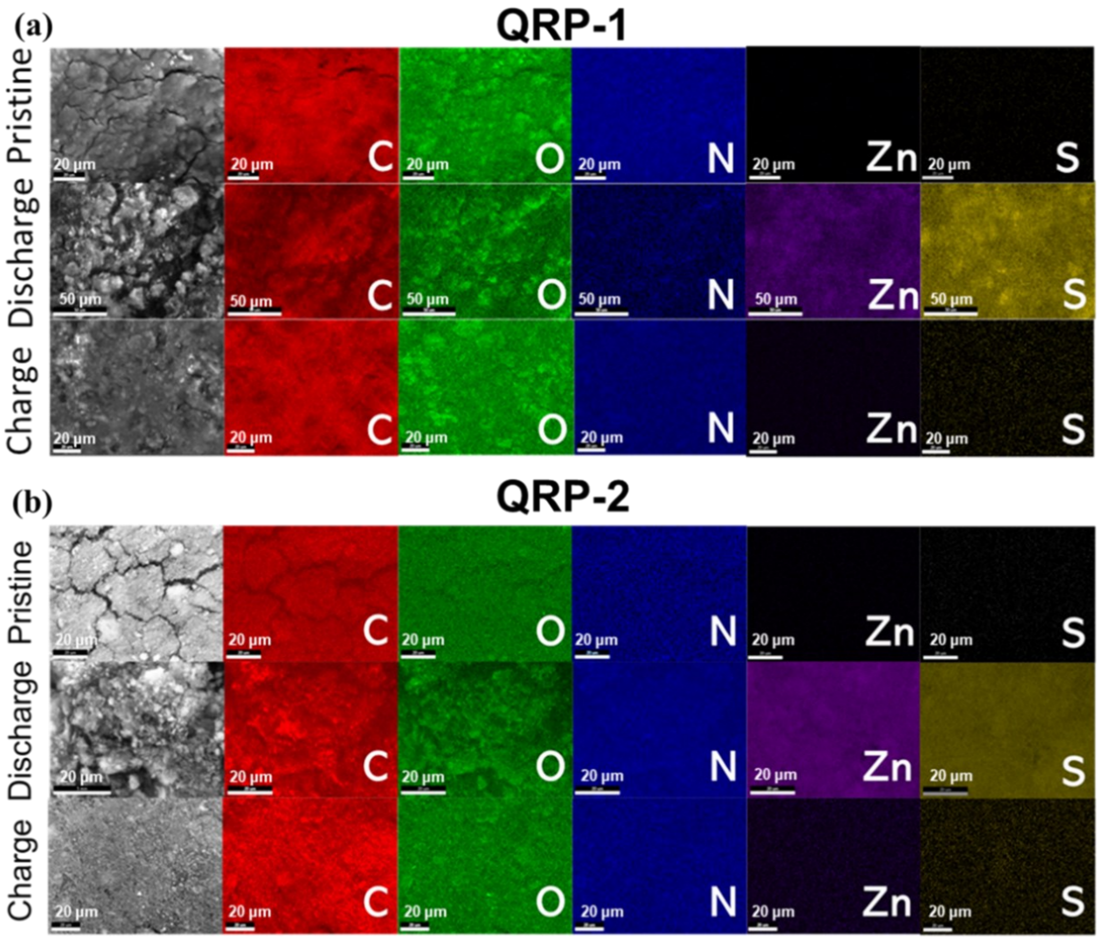

Figure 3.17. SEM/EDX analysis of (a)QRP-1 and (b)QRP-2 electrode at charged and discharged states.

Furthermore, XPS spectroscopy was conducted on the discharge/charge states of the electrodes obtained from two polymers. In the high-resolution spectra of the electrodes discharged at 0.1 V, the signals of Zn 2p and S 2p were observed. These signals were significantly reduced in the electrode at the fully charged states for both polymers. The presence of Zn 2p and S 2p signals in the charged electrodes of QRP-1 and QRP-2 indicates that the dissolution of zinc hydroxy sulfate salt is not fully complete (Figure 3.18).

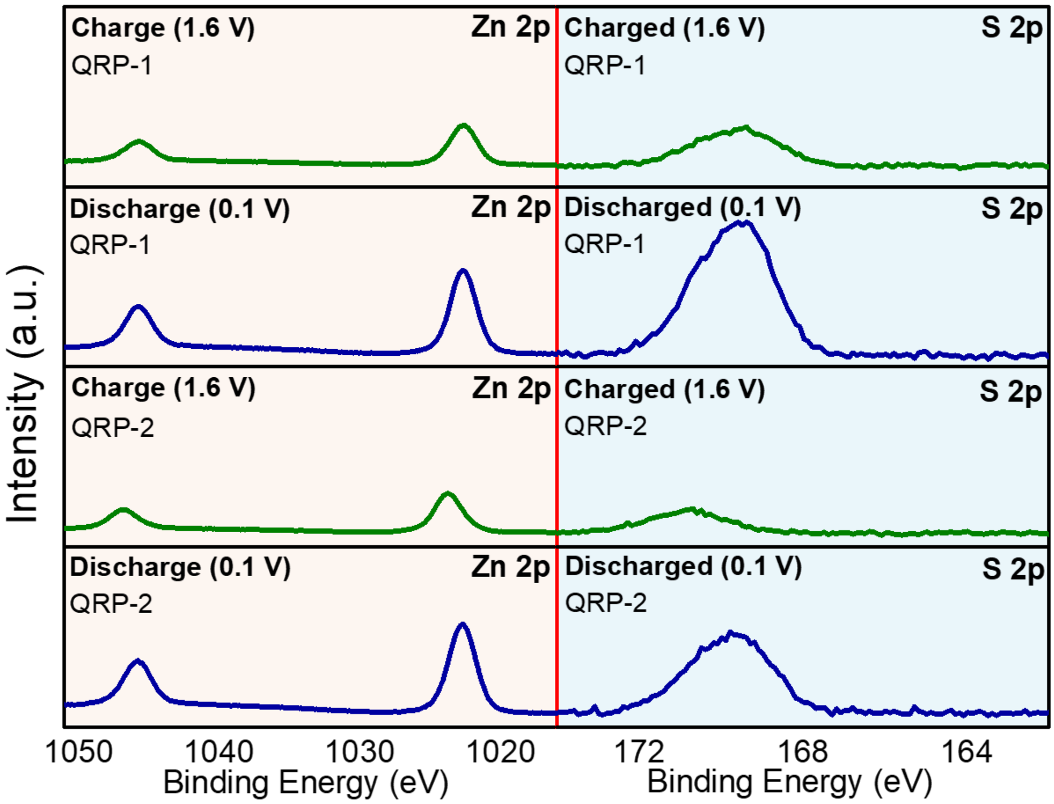

Figure 3.18. XPS analysis of QRP-1 and QRP-2 electrodes at different states.

To explore the formation of [$Zn_4SO_4(OH)_6 \cdot nH_2O$] salt and the mechanism of storing charge, the ex-situ XRD characterization was conducted. The PXRD spectra of the QRP-1 and QRP-2 cathodes in the discharge/charge stages are shown in Figure 3.19. In the literature, it has been determined that the n value in the [$Zn_4SO_4(OH)_6 \cdot nH_2O$] salt varies.[76,77].As a result, the XRD peaks of the zinc hydroxy sulfate salt appear at different positions. The peaks corresponding to [$Zn_4SO_4(OH)_6 \cdot 5H_2O$] for QRP-1 and [$Zn_4SO_4(OH)_6 \cdot 3H_2O$] for QRP-2 exhibit a decrease when the electrode is in the charging state at 1.6 V and increased while the electrode is discharging at 0.1 V. This observation matches the findings gathered from the FTIR, XPS, and EDX investigations of the charged electrode. Moreover, the reversible nature of the process of the forming of [$Zn_4SO_4(OH)_6 \cdot nH_2O$] is verified by the reappearance of the unique XRD peak of [$Zn_4SO_4(OH)_6 \cdot nH_2O$] salt when the electrode is charged and discharged again.

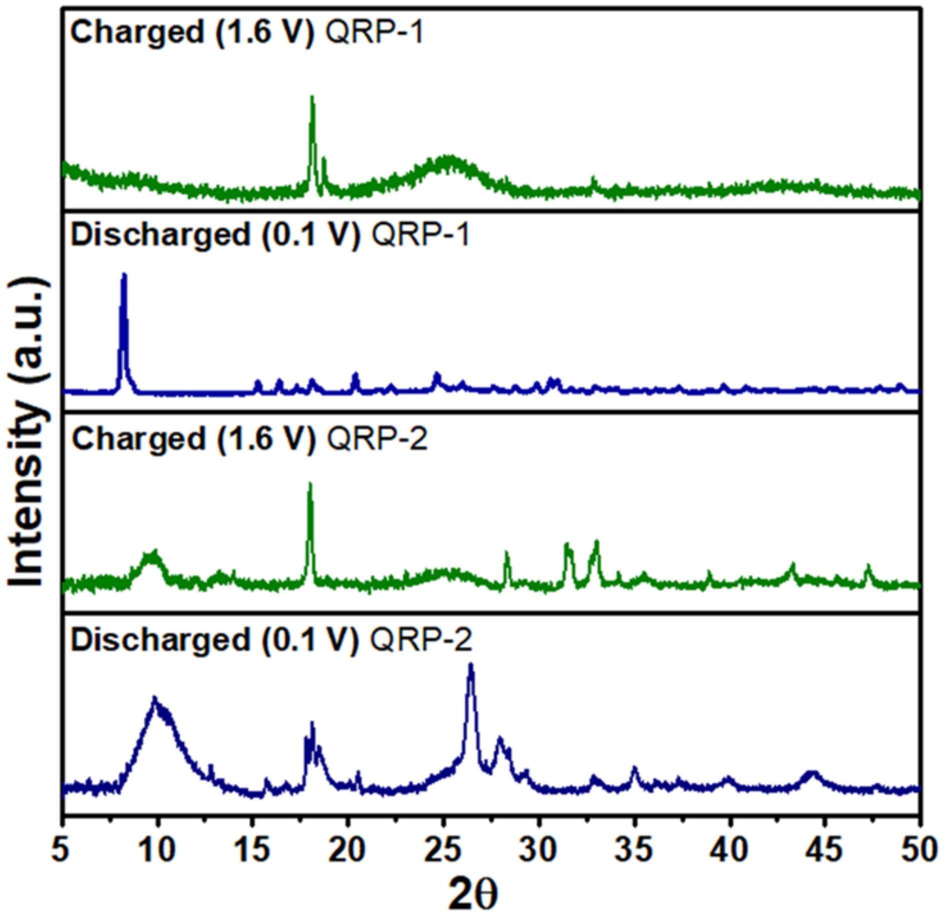

Figure 3.19. XPS analysis of QRP-1 and QRP-2 electrodes at 1.6 V and 0.1 V.

CHAPTER 4

CONCLUSION

In conclusion, quinone/pyrrole-based redox-active polymers (QRP-1 and QRP-2) were synthesized using pyrrole and quinone derivatives as starting materials. The synthesized polymers are used as a cathode material for zinc-ion batteries (ZIBs). The successful synthesis of the QRP-1 and QRP-2 was confirmed by the utilization of FT-IR and XPS spectroscopic techniques. The structure of both QRP-1 and QRP-2 allowed zinc and proton ions to efficiently reach the redox-active sites of the proposed structures. Using QRP-1 and QRP-2 as cathodes, the cells achieved discharge capacities of 180 mA h g^{-1} and 134 mA h g^{-1}, respectively, at 0.1 mA g^{-1}. QRPs maintained long-term cycling stability over 10000 cycles at 2.0 A g^{-1}, with final specific capacities of 42 mA h g^{-1} for QRP-1 and 104 mA h g^{-1} for QRP-2. This study reveals the potential of conjugated polymers (CP) as a cathode material in ZIBs. We anticipate these findings will inspire researchers to develop and investigate additional conjugated organic polymers as cathode materials for ZIBs.

REFERENCES

1. Petinrin, J. O.; Shaaban, M. Renewable energy for continuous energy sustainability in Malaysia. *Renew. Sustain. Energy Rev.* **2015**, *50*, 967-981. DOI: 10.1016/j.rser.2015.04.146

2. Michaelides, E. E. Decarbonization of the electricity generation sector and its effects on sustainability goals. *Sustainable Energy res.* **2023**, *10* (1), 10. DOI: 10.1186/s40807-023-00080-1

3. Scrosati, B.; Hassoun, J.; Sun, Y.-K. Lithium-ion batteries. A look into the future. *Energy Environ. Sci*. **2011,** *4* (9), 3287-3295, DOI: 10.1039/C1EE01388B

4. Sridhar, S.; Salkuti, S. R. Development and Future Scope of Renewable Energy and Energy Storage Systems. *Smart Cities*, **2022**, *5*, 668-699. DOI: 10.3390/smartcities5020035

5. Guarnieri, M. Secondary Batteries for Mobile Applications: From Lead to Lithium [Historical]. *IEEE Ind. Electron. Mag.* **2022**, *16* (4), 60-68. DOI: 10.1109/MIE.2022.3212242

6. Li, M.; Lu, J.; Chen, Z.; Amine, K. 30 Years of Lithium-Ion Batteries. *Adv. Mater.* **2018**, *30* (33), 1800561. DOI: 10.1002/adma.201800561

7. Gao, M.; Pan, S.-Y.; Chen, W.-C.; Chiang, P.-C. A cross-disciplinary overview of naturally derived materials for electrochemical energy storage. *Mater. Today Energy* **2018**, *7*, 58-79. DOI: 10.1016/j.mtener.2017.12.005

8. Manthiram, A. An Outlook on Lithium Ion Battery Technology. *ACS Cent. Sci.* **2017**, *3* (10), 1063-1069. DOI: 10.1021/acscentsci.7b00288

9. Liu, Y.; Zhang, R.; Wang, J.; Wang, Y. Current and future lithium-ion battery manufacturing. *iScience*, **2021**, *24* (4), 102332. DOI: 10.1016/j.isci.2021.102332

10. Li, W.; Li, H.; He, Z.; Ji, W.; Zeng, J.; Li, X.; Zhang, Y.; Zhang, P.; Zhao, J. Electrochemical Failure Results Inevitable Capacity Degradation in Li-Ion Batteries—A Review. In *Energies*, 2022; Vol. 15. DOI: 10.3390/en15239165

11. Wang, Q.; Ping, P.; Zhao, X.; Chu, G.; Sun, J.; Chen, C. Thermal runaway caused fire and explosion of lithium ion battery. *J. Power Sources,* **2012**, *208*, 210-224. DOI: 10.1016/j.jpowsour.2012.02.038

12. Costa, C. M.; Barbosa, J. C.; Gonçalves, R.; Castro, H.; Campo, F. J. D.; Lanceros-Méndez, S. Recycling and environmental issues of lithium-ion batteries: Advances, challenges and opportunities. *Energy Storage Mater.* **2021**, *37*, 433-465. DOI: 10.1016/j.ensm.2021.02.032

13. Jaguemont, J.; Bardé, F. A critical review of lithium-ion battery safety testing and standards. *Appl. Therm. Eng.* **2023**, *231*, 121014. DOI: 10.1016/j.applthermaleng.2023.121014

14. Liu, S.; Zhang, R.; Wang, C.; Mao, J.; Chao, D.; Zhang, C.; Zhang, S.; Guo, Z. Zinc ion Batteries: Bridging the Gap from Academia to Industry for Grid-Scale Energy Storage. *Angew. Chem. Int. Ed.* **2024**, *63* (17), e202400045. DOI: 10.1002/anie.202400045

15. Gourley, S. W. D.; Brown, R.; Adams, B. D.; Higgins, D. Zinc-ion batteries for stationary energy storage. *Joule* **2023**, *7* (7), 1415-1436. DOI: 10.1016/j.joule.2023.06.007

16. Zhang, N.; Chen, X.; Yu, M.; Niu, Z.; Cheng, F.; Chen, J. Materials chemistry for rechargeable zinc-ion batteries. *Chem. Soc. Rev.* **2020**, *49* (13), 4203-4219. DOI: 10.1039/C9CS00349E

17. Chen, L.; An, Q.; Mai, L. Recent Advances and Prospects of Cathode Materials for Rechargeable Aqueous Zinc-Ion Batteries. *Adv. Mater. Interfaces*, **2019**, *6* (17), 1900387. DOI: 10.1002/admi.201900387

18. Zhou, X.; Jiang, S.; Zhu, S.; Xiang, S.; Zhang, Z.; Xu, X.; Xu, Y.; Zhou, J.; Tan, S.; Pan, Z.; et al. The progress of cathode materials in aqueous zinc-ion batteries. *Nanotechnol. Rev.* **2023**, *12* (1). DOI: 10.1515/ntrev-2023-0122

19. Jiahao, L.; Hanfeng, L. Organic cathode materials for aqueous zinc-organic batteries. *Energy Mater.* **2024**, *4* (3), 400033. DOI: 10.20517/energymater.2023.116

20. Yang, J.; Hua, H.; Yang, H.; Lai, P.; Zhang, M.; Lv, Z.; Wen, Z.; Li, C. C.; Zhao, J.; Yang, Y. A High Utilization and Environmentally Sustainable All-Organic Aqueous Zinc-Ion Battery Enabled by a Molecular Architecture Design. *Adv. Energy Mater.* **2023**, *13* (25), 2204005. DOI: 10.1002/aenm.202204005

21. Guo, X.; He, G. Opportunities and challenges of zinc anodes in rechargeable aqueous batteries. *J. Mater. Chem. A,* **2023**, *11* (23), 11987-12001. DOI: 10.1039/D3TA01904G

22. Chen, D.; Lu, M.; Cai, D.; Yang, H.; Han, W. Recent advances in energy storage mechanism of aqueous zinc-ion batteries. *J. Energy Chem.* **2021**, *54*, 712-726. DOI: 10.1016/j.jechem.2020.06.016

23. Zhang, T.; Tang, Y.; Fang, G.; Zhang, C.; Zhang, H.; Guo, X.; Cao, X.; Zhou, J.; Pan, A.; Liang, S. Electrochemical Activation of Manganese-Based Cathode in Aqueous Zinc-Ion Electrolyte. *Adv. Funct. Mater.* **2020**, *30* (30), 2002711. DOI: 10.1002/adfm.202002711

24. Fenta, F. W.; Olbasa, B. W.; Tsai, M.-C.; Weret, M. A.; Zegeye, T. A.; Huang, C.-J.; Huang, W.-H.; Zeleke, T. S.; Sahalie, N. A.; Pao, C.-W.; et al. Electrochemical transformation reaction of Cu–MnO in aqueous rechargeable zinc-ion batteries for high performance and long cycle life. *J. Mater. Chem.* A, **2020**, *8* (34), 17595-17607 DOI: 10.1039/D0TA04175K

25. Zhang, N.; Wang, J.-C.; Guo, Y.-F.; Wang, P.-F.; Zhu, Y.-R.; Yi, T.-F. Insights on rational design and energy storage mechanism of Mn-based cathode materials towards high performance aqueous zinc-ion batteries. *Coord. Chem. Rev.* **2023**, *479*, 215009. DOI: 10.1016/j.ccr.2022.215009

26. Ren, J.; Wang, Z.; Xu, P.; Wang, C.; Gao, F.; Zhao, D.; Liu, S.; Yang, H.; Wang, D.; Niu, C.; et al. Porous Co2VO4 Nanodisk as a High-Energy and Fast-Charging Anode for Lithium-Ion Batteries. *Nano-Micro Lett.* **2021**, *14* (1), 5. DOI: 10.1007/s40820-021-00758-5

27. Hurlbutt, K.; Wheeler, S.; Capone, I.; Pasta, M. Prussian Blue Analogs as Battery Materials. *Joule* **2018**, *2* (10), 1950-1960. DOI: 10.1016/j.joule.2018.07.017

28. Peng, J.; Zhang, W.; Liu, Q.; Wang, J.; Chou, S.; Liu, H.; Dou, S. Prussian Blue Analogues for Sodium-Ion Batteries: Past, Present, and Future. *Adv. Mater.* **2022**, *34* (15), 2108384. DOI: 10.1002/adma.202108384

29. Li, X.; Huang, Z.; Shuck, C. E.; Liang, G.; Gogotsi, Y.; Zhi, C. MXene chemistry, electrochemistry and energy storage applications. *Nat. Rev. Chem.* **2022**, *6* (6), 389-404. DOI: 10.1038/s41570-022-00384-8

30. Zhang, L.; Chen, Y.; Jiang, Z.; Chen, J.; Wei, C.; Wu, W.; Li, S.; Xu, Q. Cation-Anion Redox Active Organic Complex for High Performance Aqueous Zinc Ion Battery. *Energy Environ. Mater.* **2024**, *7* (1), e12507. DOI: 10.1002/eem2.12507

31. Geng, X.; Jiang, Y.; Ma, H.; Zhang, H.; Liu, J.; Zhang, Z.; Peng, C.; Zhang, J.; Zhao, Q.; Zhu, N. Long-Life Aqueous Zinc-Ion Batteries of Organic Iminodianthraquinone/rGO Cathode Assisted by Zn2+ Binding with Adjacent Molecules. *ACS Appl. Mater. Interfaces.* **2022**, *14* (44), 49746-49754. DOI: 10.1021/acsami.2c13261

32. Zhao, Q.; Huang, W.; Luo, Z.; Liu, L.; Lu, Y.; Li, Y.; Li, L.; Hu, J.; Ma, H.; Chen, J. High-capacity aqueous zinc batteries using sustainable quinone electrodes. *Sci. adv.* **2018***, 4* (3), eaao1761. DOI: 10.1126/sciadv.aao1761

33. Lin, Z.; Shi, H.-Y.; Lin, L.; Yang, X.; Wu, W.; Sun, X. A high capacity small molecule quinone cathode for rechargeable aqueous zinc-organic batteries. *Nat. Commun.* **2021**, *12* (1), 4424. DOI: 10.1038/s41467-021-24701-9

34. Kumankuma-Sarpong, J.; Tang, S.; Guo, W.; Fu, Y. Naphthoquinone-Based Composite Cathodes for Aqueous Rechargeable Zinc-Ion Batteries. *ACS Appl. Mater. Interfaces.* **2021**, *13* (3), 4084-4092. DOI: 10.1021/acsami.0c21339

35. Kundu, D.; Oberholzer, P.; Glaros, C.; Bouzid, A.; Tervoort, E.; Pasquarello, A.; Niederberger, M. Organic Cathode for Aqueous Zn-Ion Batteries: Taming a Unique Phase Evolution toward Stable Electrochemical Cycling. *Chem. Mater.* **2018**, *30* (11), 3874-3881. DOI: 10.1021/acs.chemmater.8b01317

36. Guo, Z.; Ma, Y.; Dong, X.; Huang, J.; Wang, Y.; Xia, Y. An Environmentally Friendly and Flexible Aqueous Zinc Battery Using an Organic Cathode. *Angew. Chem. Int. Ed.* **2018**, *57* (36), 11737-11741. DOI: 10.1002/anie.201807121

37. Wang, X.; Chen, L.; Lu, F.; Liu, J.; Chen, X.; Shao, G. Boosting Aqueous Zn2+ Storage in 1,4,5,8-Naphthalenetetracarboxylic Dianhydride through Nitrogen Substitution. *ChemElectroChem* **2019**, *6* (14), 3644-3647. DOI: 10.1002/celc.201900750

38. C´iric´-Marjanovic´, G.; Mentus, S. Charge–discharge characteristics of polythiopheneas a cathode active material in a rechargeable battery. *J. Appl. Electrochem.* **1998**, *28* (1), 103-106. DOI: 10.1023/A:1003210220871

39. Wang, Y.; Wang, C.; Ni, Z.; Gu, Y.; Wang, B.; Guo, Z.; Wang, Z.; Bin, D.; Ma, J.; Wang, Y. Binding Zinc Ions by Carboxyl Groups from Adjacent Molecules toward Long-Life Aqueous Zinc–Organic Batteries. *Adv. Mater.* **2020**, *32* (16), 2000338. DOI: 10.1002/adma.202000338

40. Sun, T.; Zhang, W.; Nian, Q.; Tao, Z. Molecular Engineering Design for High-Performance Aqueous Zinc-Organic Battery. *Nano-Micro Lett.* **2023**, *15* (1), 36. DOI: 10.1007/s40820-022-01009-x

41. Gao, Y.; Li, G.; Wang, F.; Chu, J.; Yu, P.; Wang, B.; Zhan, H.; Song, Z. A high-performance aqueous rechargeable zinc battery based on organic cathode integrating quinone and pyrazine. *Energy Storage Mater.* **2021**, *40*, 31-40. DOI: 10.1016/j.ensm.2021.05.002

42. Shi, Y.; Wang, P.; Gao, H.; Jin, W.; Chen, Y.; Huang, Y.; Wu, T.-R.; Wu, D.-Y.; Xu, J.; Cao, J. π-Conjugated N-heterocyclic compound with redox-active quinone and pyrazine moieties as a high-capacity organic cathode for aqueous zinc-ion batteries. *Chem. Eng. J.* **2023**, *461*, 141850. DOI: 10.1016/j.cej.2023.141850

43. Sun, T.; Zhang, W.; Zha, Z.; Cheng, M.; Li, D.; Tao, Z. Designing a solubility-limited small organic molecule for aqueous zinc-organic batteries. *Energy Storage Mater.* **2023**, *59*, 102778. DOI: 10.1016/j.ensm.2023.102778

44. Huang, L.; Li, J.; Wang, J.; Lv, H.; Liu, Y.; Peng, B.; Chen, L.; Guo, W.; Wang, G.; Gu, T. Organic Compound as a Cathode for Aqueous Zinc-Ion Batteries with Improved Electrochemical Performance via Multiple Active Centers. *ACS Appl. Energy Mater.* **2022**, *5* (12), 15780-15787. DOI: 10.1021/acsaem.2c03338

45. Sun, T.; Yi, Z.; Zhang, W.; Nian, Q.; Fan, H. J.; Tao, Z. Dynamic Balance of Partial Charge for Small Organic Compound in Aqueous Zinc-Organic Battery. *Adv. Funct. Mater.* **2023**, *33* (47), 2306675. DOI: 10.1002/adfm.202306675

46. Wang, Q.; Liu, Y.; Chen, P. Phenazine-based organic cathode for aqueous zinc secondary batteries. *J. Power Sources* **2020**, *468*, 228401. DOI: 10.1016/j.jpowsour.2020.228401

47. Liang, J.; Tang, M.; Cheng, L.; Zhu, Q.; Ji, R.; Liu, X.; Zhang, Q.; Wang, H.; Liu, Z. 2,3-diaminophenazine as a high-rate rechargeable aqueous zinc-ion batteries cathode. *J. Colloid Interface Sci.* **2022**, *607*, 1262-1268. DOI: 10.1016/j.jcis.2021.09.072

48. Tie, Z.; Liu, L.; Deng, S.; Zhao, D.; Niu, Z. Proton Insertion Chemistry of a Zinc–Organic Battery. *Angew. Chem. Int. Ed.* **2020**, *59* (12), 4920-4924. DOI: 10.1002/anie.201916529

49. Li, W.; Xu, H.; Zhang, H.; Wei, F.; Huang, L.; Ke, S.; Fu, J.; Jing, C.; Cheng, J.; Liu, S. Tuning electron delocalization of hydrogen-bonded organic framework cathode for high-performance zinc-organic batteries. *Nat. Commun.* **2023**, *14* (1), 5235. DOI: 10.1038/s41467-023-40969-5

50. Ye, Z.; Xie, S.; Cao, Z.; Wang, L.; Xu, D.; Zhang, H.; Matz, J.; Dong, P.; Fang, H.; Shen, J.; et al. High-rate aqueous zinc-organic battery achieved by lowering HOMO/LUMO of organic cathode. *Energy Storage Mater.* **2021**, *37*, 378-386. DOI: 10.1016/j.ensm.2021.02.022

51. Li, S.; Shang, J.; Li, M.; Xu, M.; Zeng, F.; Yin, H.; Tang, Y.; Han, C.; Cheng, H.-M. Design and Synthesis of a π-Conjugated N-Heteroaromatic Material for Aqueous Zinc–Organic Batteries with Ultrahigh Rate and Extremely Long Life. *Adv. Mater.* **2023**, *35* (50), 2207115. DOI: 10.1002/adma.202207115

52. Jiménez, P.; Levillain, E.; Alévêque, O.; Guyomard, D.; Lestriez, B.; Gaubicher, J. Lithium n-Doped Polyaniline as a High-Performance Electroactive Material for Rechargeable Batteries. *Angew. Chem. Int. Ed.* **2017**, *56* (6), 1553-1556. DOI: 10.1002/anie.201607820

53. Das, S.; Heasman, P.; Ben, T.; Qiu, S. Porous Organic Materials: Strategic Design and Structure–Function Correlation. *Chem. Rev.* **2017**, *117* (3), 1515-1563. DOI: 10.1021/acs.chemrev.6b00439

54. An, Y.; Tan, S.; Liu, Y.; Zhu, K.; Hu, L.; Rong, Y.; An, Q. Designs and applications of multi-functional covalent organic frameworks in rechargeable batteries. *Energy Storage Mater.* **2021**, *41*, 354-379. DOI: 10.1016/j.ensm.2021.06.010

55. Patel, H. A.; Hyun Je, S.; Park, J.; Chen, D. P.; Jung, Y.; Yavuz, C. T.; Coskun, A. Unprecedented high-temperature CO2 selectivity in N2-phobic nanoporous covalent organic polymers. *Nat. Commun.* **2013**, *4* (1), 1357. DOI: 10.1038/ncomms2359

56. Yang, D.-H.; Tao, Y.; Ding, X.; Han, B.-H. Porous organic polymers for electrocatalysis. *Chem. Soc. Rev.* **2022**, *51* (2), 761-791, DOI: 10.1039/D1CS00887K

57. Wang, S.; Li, H.; Huang, H.; Cao, X.; Chen, X.; Cao, D. Porous organic polymers as a platform for sensing applications. *Chem. Soc. Rev.* **2022**, *51* (6), 2031-2080, DOI: 10.1039/D2CS00059H

58. Mohamed, M. G.; El-Mahdy, A. F. M.; Kotp, M. G.; Kuo, S.-W. Advances in porous organic polymers: syntheses, structures, and diverse applications. *Mater. Adv.* **2022**, *3* (2), 707-733, DOI: 10.1039/D1MA00771H

59. Wang, Y.; Wang, X.; Tang, J.; Tang, W. A quinoxalinophenazinedione covalent triazine framework for boosted high-performance aqueous zinc-ion batteries. *J. Mater. Chem. A* **2022**, *10* (26), 13868-13875, DOI: 10.1039/D2TA03655J

60. Buyukcakir, O.; Yuksel, R.; Begar, F.; Erdogmus, M.; Arsakay, M.; Lee, S. H.; Kim, S. O.; Ruoff, R. S. Ultralong-Life Quinone-Based Porous Organic Polymer Cathode for High-Performance Aqueous Zinc-Ion Batteries. *ACS Appl. Energy Mater.* **2023**, *6* (14), 7672-7680. DOI: 10.1021/acsaem.3c01163

61. Zheng, S.; Shi, D.; Yan, D.; Wang, Q.; Sun, T.; Ma, T.; Li, L.; He, D.; Tao, Z.; Chen, J. Orthoquinone–Based Covalent Organic Frameworks with Ordered Channel Structures for Ultrahigh Performance Aqueous Zinc–Organic Batteries. *Angew. Chem. Int. Ed.* **2022**, *61* (12), e202117511. DOI: 10.1002/anie.202117511

62. Wang, W.; Kale, V. S.; Cao, Z.; Lei, Y.; Kandambeth, S.; Zou, G.; Zhu, Y.; Abouhamad, E.; Shekhah, O.; Cavallo, L.; et al. Molecular Engineering of Covalent Organic Framework Cathodes for Enhanced Zinc-Ion Batteries. *Adv. Mater.* **2021**, *33* (39), 2103617. DOI: 10.1002/adma.202103617

63. Khayum M, A.; Ghosh, M.; Vijayakumar, V.; Halder, A.; Nurhuda, M.; Kumar, S.; Addicoat, M.; Kurungot, S.; Banerjee, R. Zinc ion interactions in a two-dimensional covalent organic framework based aqueous zinc ion battery. *Chem. Sci.* **2019**, *10* (38), 8889-8894, DOI: 10.1039/C9SC03052B

64. Wang, W.; Kale, V. S.; Cao, Z.; Kandambeth, S.; Zhang, W.; Ming, J.; Parvatkar, P. T.; Abou-Hamad, E.; Shekhah, O.; Cavallo, L.; et al. Phenanthroline Covalent Organic Framework Electrodes for High-Performance Zinc-Ion Supercapattery. *ACS Energy Lett.* **2020**, *5* (7), 2256-2264. DOI: 10.1021/acsenergylett.0c00903

65. Wang, X.; Xiao, J.; Tang, W. Hydroquinone versus Pyrocatechol Pendants Twisted Conjugated Polymer Cathodes for High-Performance and Robust Aqueous Zinc-Ion Batteries. *Adv. Funct. Mater.* **2022**, *32* (4), 2108225. DOI: 10.1002/adfm.202108225

66. Zhang, H.; Zhong, L.; Xie, J.; Yang, F.; Liu, X.; Lu, X. A COF-Like N-Rich Conjugated Microporous Polytriphenylamine Cathode with Pseudocapacitive Anion Storage Behavior for High-Energy Aqueous Zinc Dual-Ion Batteries. *Adv. Mater.* **2021**, *33* (34), 2101857. DOI: 10.1002/adma.202101857

67. Liang, Y.; Xia, Y.; Wang, X.; Zhou, J. An imine-rich polymer with enlarged π-conjugated planes for aqueous zinc-ion batteries. *Chem. Commun.* **2023**, *59* (86), 12927-12930, DOI: 10.1039/D3CC04436J

68. Wang, X.; Tang, J.; Tang, W. Manipulating Polymer Configuration to Accelerate Cation Intercalation Kinetics for High-Performance Aqueous Zinc-Ion Batteries. *Adv. Funct. Mater.* **2022**, *32* (27), 2200517. DOI: 10.1002/adfm.202200517

69. Ye, F.; Liu, Q.; Dong, H.; Guan, K.; Chen, Z.; Ju, N.; Hu, L. Organic Zinc-Ion Battery: Planar, π-Conjugated Quinone-Based Polymer Endows Ultrafast Ion Diffusion Kinetics. *Angew. Chem. Int. Ed.* **2022**, *61* (51), e202214244. DOI: 10.1002/anie.202214244

70. Wang, J.; Wang, J.-G.; Qin, X.; Wang, Y.; You, Z.; Liu, H.; Shao, M. Superfine MnO2 Nanowires with Rich Defects Toward Boosted Zinc Ion Storage Performance. *ACS Appl. Mater. Interfaces.* **2020**, *12* (31), 34949-34958. DOI: 10.1021/acsami.0c08812

71. Li, Z.; Tan, J.; Zhu, X.; Xie, S.; Fang, H.; Ye, M.; Shen, J. High capacity and long-life aqueous zinc-ion battery enabled by improving active sites utilization and protons insertion in polymer cathode. *Energy Storage Mater.* **2022**, *51*, 294-305. DOI: 10.1016/j.ensm.2022.06.049

72. Fritz, P. W.; Chen, T.; Ashirov, T.; Nguyen, A.-D.; Dincă, M.; Coskun, A. Fully Conjugated Tetraoxa[8]circulene-Based Porous Semiconducting Polymers. *Angew. Chem. Int. Ed.* **2022**, *61* (17), e202116527. DOI: 10.1002/anie.202116527

73. Chu, J.; Li, G.; Wang, Y.; Zhang, X.; Yang, Z.; Han, Y.; Cai, T.; Song, Z. Benzoquinone–Pyrrole Polymers as Cost-Effective Cathodes toward Practical Organic Batteries. *ACS Appl. Mater. Interfaces.* **2022**, *14* (22), 25566-25575. DOI: 10.1021/acsami.2c05703

74. Liu, J.; Wang, J.; Xu, C.; Jiang, H.; Li, C.; Zhang, L.; Lin, J.; Shen, Z. X. Advanced Energy Storage Devices: Basic Principles, Analytical Methods, and Rational Materials Design. *Adv. Sci.* **2018**, *5* (1), 1700322. DOI: 10.1002/advs.201700322

75. Lim, W.-G.; Li, X.; Reed, D. Understanding the Role of Zinc Hydroxide Sulfate and its Analogues in Mildly Acidic Aqueous Zinc Batteries: A Review. *Small Methods* **2024**, *8* (6), 2300965. DOI: 10.1002/smtd.202300965

76. Kundu, D.; Hosseini Vajargah, S.; Wan, L.; Adams, B.; Prendergast, D.; Nazar, L. F. Aqueous vs. nonaqueous Zn-ion batteries: consequences of the desolvation penalty at the interface. *Energy Environ. Sci.* **2018**, *11* (4), 881-892, DOI: 10.1039/C8EE00378E

77. Keleş Güner, E.; Akkaş, R.; Özer, A. Synthesis of zinc sulfate hydroxide trihydrate by chemical precipitation and its transformation to zinc oxide. *Chem. Eng. Commun.* **2022**, *209* (9), 1203-1213. DOI: 10.1080/00986445.2021.1953486

APPENDIX A

^{1}H-NMR AND ^{13}C-NMR SPECTRA OF COMPOUND

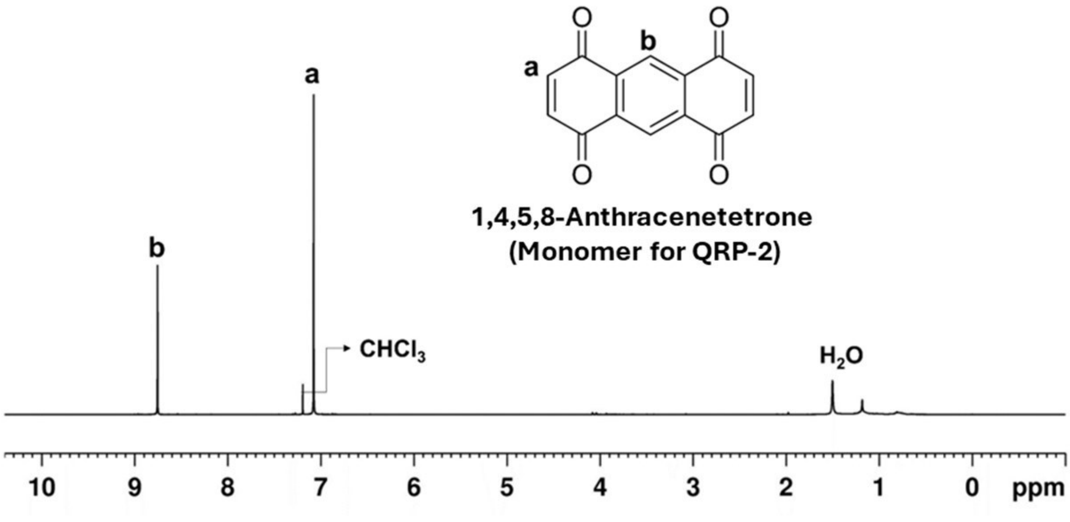

Figure A. 1. ^{1}H-NMR spectrum of QRP-2 Monomer (1,4,5,8-Anthracenetetrone).

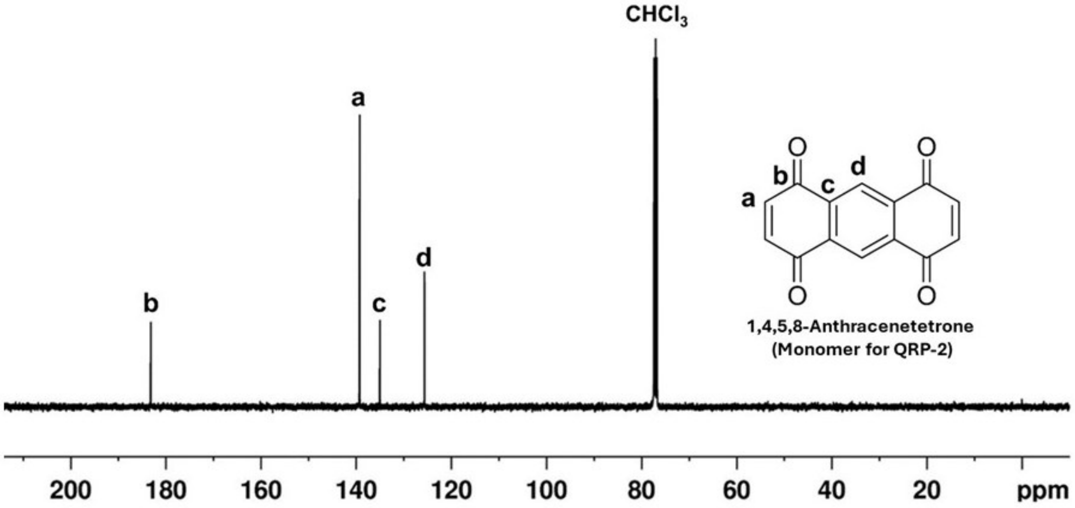

Figure A. 2. ^{13}C-NMR spectrum of QRP-2 Monomer (1,4,5,8-Anthracenetetrone).